Benthic alkalinity and DIC fluxes in the Rhône River prodelta generated by decoupled aerobic and anaerobic processes

Jens Rassmann[a,1], Eryn M. Eitel[b,1], Bruno Lansard[a] , Cécile Cathalot[c], Christophe Brandily[c], Martial Taillefert[b] , Christophe Rabouille[a, 2]

[a] *Laboratoire des Sciences du Climat et de l'Environnement, LSCE/IPSL,CEA-CNRS-UVSQ-Université Paris Saclay, 91198 Gif-sur-Yvette, France*

[b] *School of Earth and Atmospheric Sciences; Georgia Institute of Technology, GA 30332-0340 Atlanta, USA*

[c] *IFREMER, Laboratoire Environnement Profond, 29280 Plouzané, France*

[1] Jens Rassmann and Eryn M. Eitel contributed equally to this article

[2] Corresponding author

Email address: rabouill@lsce.ipsl.fr (Christophe Rabouille)

ORCID: https://orcid.org/0000-0003-1211-717X

1

Abstract

Estuarine regions are generally considered a major source of atmospheric CO_2 as a result of the high organic carbon (OC) mineralization rates in their water column and sediments. Yet, the intensity of anaerobic respiration processes in the sediments tempered by the reoxidation of reduced metabolites near the sediment-water interface controls the flux of benthic alkalinity. This alkalinity may partially buffer metabolic CO_2 generated by benthic OC respiration in sediments. Thus sediments with high anaerobic respiration rates could contribute less to local acidification than previously thought. In this study, a benthic chamber was deployed in the Rhône River prodelta and the adjacent continental shelf (Gulf of Lions, NW Mediterranean) in late summer to assess the fluxes of total alkalinity (TA) and dissolved inorganic carbon (DIC) from the sediment. Concurrently, *in situ* O_2 and pH microprofiles, voltammetric profiles and pore water composition were measured in surface sediments to identify the main biogeochemical processes controlling the net production of alkalinity in these sediments. Benthic TA and DIC fluxes to the water column, ranging between 14 and 74 mmol m^{-2} d^{-1} and 18 and 78 mmol m^{-2} d^{-1}, respectively, were up to 8 times higher than DOU rates (10.4 ± 0.9 mmol m^{-2} d^{-1}) close to the river mouth, but their intensity decreased offshore, as a result of the decline in OC inputs. In the zone close to the river mouth, pore water redox species indicated that TA and DIC were mainly produced by microbial sulfate and iron reduction. Despite the complete removal of sulfate from pore waters, dissolved sulfide concentrations were low and significant concentration of FeS were found indicating the precipitation and burial of iron sulfide minerals with an estimated burial flux of 12.5 mmol m^{-2} d^{-1} near the river mouth. By preventing reduced iron and sulfide reoxidation, the precipitation and burial of iron sulfide increases the alkalinity release from the sediments during the spring and summer months. Under these conditions, the sediment provides a net source of alkalinity to the bottom waters which mitigates the effect of the benthic DIC flux on the carbonate chemistry of coastal waters and weakens the partial pressure of CO_2 increase in the bottom waters that would occur if DIC was produced only.

Keywords

Coastal sediment, Carbon cycle; alkalinity flux; iron reduction; sulfate reduction; coupled element cycles, oxygen consumption.

1. Introduction

As a link between continental and marine environments, the coastal ocean plays a key role in the global carbon cycle (Bauer et al., 2013). In particular, large fluxes of dissolved and particulate organic carbon (POC) are delivered by rivers to neighbouring continental shelves (Bianchi and Allison, 2009). In fact, even though shelf regions only occupy around 7 % of the global ocean surface area (Jahnke, 2010), they account for more than 80 % of POC burial in the oceans (Hedges and Keil, 1995; Muller-Karger et al., 2005). About half of this POC is buried in river deltas and estuaries (McKee et al., 2004; Burdige, 2005). River-dominated ocean margins receive substantial amounts of allochthonous and authigenic POC that settle to the sea floor (Rabouille et al., 2001; Burdige, 2005; Andersson et al., 2006), therefore increasing the organic carbon content of the sediments and enhancing mineralization rates (Canfield et al., 1993a; Mckee et al., 2004; Muller-Karger et al., 2005; Aller et al., 2008; Burdige, 2011). These processes allow estuarine and deltaic regions to constitute a net source of CO_2 to the atmosphere (Chen and Borges, 2009, Cai, 2011). In these river-dominated margins, high sedimentation rates of material containing large concentrations of POC decrease the residence time of organic carbon in the oxic sediment layers (Hartnett et al., 1998) and increase the relative contribution of anaerobic compared to aerobic degradation pathways of organic carbon (Canfield et al., 1993a). Anaerobic respiration processes, including denitrification, dissimilatory nitrate reduction to ammonium (DNRA), manganese reduction, iron reduction, and sulfate reduction produce total alkalinity (TA; Berner, 1970; Dickson, 1981; Wolf-Gladrow et al., 2007, Table 1) that increases the buffer capacity of pore waters (Ben-Yaakov, 1973; Soetaert et al., 2007), drives the calcite and aragonite saturation state of the pore waters towards

supersaturation, and potentially triggers carbonate mineral precipitation (Gaillard et al., 1989; Mucci et al., 2000; Jørgensen and Kasten, 2006; Soetaert et al., 2007; Burdige, 2011). In turn, the precipitation of carbonate species, such as calcite and aragonite, consumes alkalinity within the sediments (Table 1, Eq. 1; Berner, 1970; Soetaert et al., 2007; Krumins et al., 2013; Brenner et al., 2016). Anaerobically produced alkalinity may also be consumed close to the sediment-water interface (SWI) by the aerobic reoxidation of reduced species such as NH_4^+, Mn^{2+}, Fe^{2+}, and dissolved sulfide (Table 1, Eq. 2-4; Jourabchi et al., 2005; Krumins et al., 2013; Brenner et al., 2016). However, the precipitation and ultimate burial of iron sulfide minerals may prevent reoxidation of dissolved sulfide and Fe^{2+} and significantly reduce alkalinity consumption in sediments. Other processes such as carbonate dissolution in surface sediments or denitrification from external sources of nitrate may also be sources of TA (Hu and Cai, 2011a). Thus, the net TA flux across the SWI depends on the type and intensity of anaerobic respiration, carbonate precipitation/dissolution, denitrification, and whether reduced species are reoxidized by dissolved oxygen after diffusion upwards or trapped in anaerobic sediment layers by precipitation (Krumins et al., 2013; Łukawska-Matuszewska and Graca 2018). The net flux of this anaerobically produced alkalinity also depends on its depth of production in the sediment and sedimentation rates. In river dominated margins, episodic floods can deposit several cm of new sediment during a short period (days to weeks) (Cathalot et al., 2010). In these conditions, the net flux of alkalinity from the sediment depends on the net balance of alkalinity production and consumption rates in the sediment and the intensity of upward alkalinity transport. As DIC is also produced by aerobic and anaerobic reactions, the net alkalinity flux across the SWI directly affects the partial pressure of CO_2 (pCO_2) in bottom waters (Andersson and Mackenzie, 2012).

To characterize the biogeochemical conditions in which sediments provide an alkalinity source to coastal waters, it is crucial to relate this reaction network to net benthic fluxes of alkalinity and dissolved inorganic carbon (DIC) measured *in situ*. A high ratio of benthic TA to DIC fluxes (> 1) would increase the buffer capacity of the bottom waters and influence the coastal carbon cycle by

increasing the storage capacity of CO_2 in coastal waters over long time scales (Thomas et al., 2009; Andersson et al., 2006; Brenner et al., 2016). The objectives of this study were to determine the magnitude of the alkalinity flux to the bottom waters from deltaic regions sediments exposed to large riverine inputs of carbon and minerals and identify the underlying biogeochemical processes responsible for the net production of alkalinity in these sediments. This study is one of the first to simultaneously quantify the spatial distribution of benthic TA and DIC fluxes, dissolved oxygen uptake (DOU) rates, burial fluxes of reduced substances, and the main biogeochemical processes involved in organic carbon mineralization in sediments. These processes were investigated along a gradient of organic carbon and mineral inputs to the sea floor in the Rhône River delta (France) before the usual flood season in late summer.

2. Study site and methods

2.1 The Rhône River delta

The Rhône River subaqueous delta, also called prodelta due to its prograding characteristics, is a wave-dominated delta located in the Gulf of Lions (France), a microtidal continental margin. The Rhône River is the main source of freshwater, suspended matter (including iron oxides), and POC to the Mediterranean Sea (Sempéré et al., 2000). The river plume is generally oriented southwestward due to the combined effects of wind forcing and the Coriolis effect (Estournel et al., 1997). The Grand Rhône River mouth is characterized by a prodeltaic lobe (Got et al., 1990) that can be divided into three main areas based on bathymetry and sedimentation rates (Got et al., 1990): the proximal domain within a 2 km radius of the river outlet, with water depths between 10 and 30 m and mean apparent accumulation rates of up to 30-40 cm yr^{-1} (Charmasson et al., 1988); the prodelta domain between 2 and 5 km with water depths ranging from 30 to 70 m and sedimentation rates of 1-4 cm yr^{-1} (Miralles et al., 2005); and the distal domain further offshore with water depths greater than 70 m and accumulation rates of 0.1 to 1 cm yr^{-1} (Miralles et al., 2005). In this part of

the Gulf of Lions, sediments are fine grained and of cohesive nature (Roussiez et al., 2005; Cathalot et al., 2013). Their total organic carbon content in surface sediments is higher than 2 % close to the river mouth and decreases offshore (Lansard et al., 2008). The sedimentary inorganic carbon content ranges between 28 and 38 % (Roussiez et al., 2005) and is, to more than 95 %, composed of calcite (Rassmann et al., 2016) originating from the calcareous belt around the Alps. The other 5 % are aragonite and magnesian calcite. The sediments of the three domains are characterized by a strong biogeochemical gradient from the Rhône River mouth to the Gulf of Lions continental slope leading to large sediment respiration rates in the proximal domain that decrease offshore (Lansard et al., 2009; Pastor et al., 2011; Cathalot et al., 2013; Rassmann et al., 2016). These sediments are characterized by strong anaerobic production of TA and DIC (Rassmann et al., 2016), but whether this alkalinity is consumed in the oxic sediment layer or released to the bottom waters has yet to be determined.

Most of the Rhône River particles are deposited in the proximal and prodelta areas during flood events (80 % of the particles; Maillet et al., 2006; Cathalot et al., 2010; Zebracki et al., 2015), mainly in late fall and early winter, leading to the periodic accumulation of terrestrial organic-rich particles in these sediments (Radakovich et al., 1999; Roussiez et al., 2005). A large proportion of this terrestrial organic matter (>90%; Lansard et al., 2009; Cathalot et al., 2013) with occasional coarse particles (CPOM, Charles et al., 2014) is mineralized in the spring and summer. Although data are scarce, metabolites from carbon remineralization processes probably build-up progressively during winter and spring (Rassmann, unpublished data). This temporal evolution yields similar diagenetic signatures from mid-spring to end of summer, including almost complete sulfate reduction, large concentration of DIC and alkalinity (30-40 mM), 500-800 µM of dissolved iron, and no dissolved sulfide in the pore waters (Rassmann et al., 2016; Pastor et al., 2011). This pattern was observed consistently over several sampling campaigns, including April 2007 (Pastor et al., 2011), April 2013 (Dumoulin et al., 2018), May 2014 (Rassmann et al., 2016), September 2015 (this paper), and May 2018 (unpublished results). Altogether, the pore water data collected over the

126 years in the Rhône prodelta system are consistent and indicate that biogeochemical processes in the
127 critical proximal zone reach a reproducible state on a yearly basis due to the regularity of flood
128 deposition in late fall and maturation of the system in spring and summer. This reproducibility of
129 the spring-summer conditions probably also applies to benthic fluxes.

130

131

132 *2.2 Bottom water sampling and analyses*

133 The AMOR-B-Flux cruise took place on-board the RV Tethys II (CNRS-INSU) in September
134 2015. The investigated stations were located in the river plume along a nearshore-offshore transect
135 (Fig. 1 and Table 2). Bottom water samples were collected with 12-L Niskin® bottles from 1-2 m
136 above the sea floor. The sampling depth was checked with a mounted underwater depth gauge. The
137 seawater temperature was measured using a thermometer with a precision of 0.1 °C and the salinity
138 with a conductivity based thermosalinometer with a precision of 0.1. Dissolved oxygen
139 concentrations were analysed by Winkler titration (Grasshoff et al., 1983) within twelve hours after
140 sampling with a precision of ± 0.5 µM. Triplicate pH measurements were carried out at 25°C within
141 1 hour after sampling by spectrophotometry with unpurified m-cresol purple as indicator dye
142 (Clayton and Byrne, 1993) and a precision of ± 0.01 pH units. The CO2SYS software (Pierrot et al.,
143 2006, Orr et al., 2018) was used with the equilibrium constants from Luecker et al. (2000) and DIC
144 and pH as input parameters to report pH on the total proton scale (pH_T) and at *in situ* temperature
145 and salinity. As silicate and phosphate concentrations were not measured in the bottom waters,
146 average concentrations for the Gulf of Lions were used. To obtain concentrations as close as
147 possible to the seafloor, overlying water from the sediment cores was also sampled and analysed for
148 TA and DIC concentrations.

149 *2.3 In situ benthic chamber deployments*

150 Benthic fluxes were determined with an autonomous benthic lander (Jahnke and Christiansen,
151 1989). The lander was equipped with a single benthic chamber and water syringe sampling system.
152 The chamber encloses a 30 x 30 cm sediment surface area with a volume of overlying water
153 determined by measuring the initial concentration of two tracers (iodide and bromide) injected after
154 closure of the chamber within 20 minutes after deployment on the seafloor, to ensure that the
155 chamber and particles eventually resuspended were settled in the sediment. A mechanical stirrer
156 integrated in the chamber lid was run at 10 rpm to homogenize the overlying waters in the chamber
157 without interfering with sediment-water exchange processes (Buchholtz-Ten Brink et al., 1989). TA
158 and DIC samples were collected as a function of time and their concentrations corrected for the
159 dilution that occurred by replacing the sample volume collected by ambient water. The slopes of the
160 concentration-time plots were estimated using the "lm" function in R, a restricted maximum
161 likelihood estimator (REML) that takes uncertainties of individual measurements into account.
162 Finally, benthic fluxes across the SWI (F_i in mmol m^{-2} d^{-1}) were calculated from the slopes of these
163 concentration-time-plots and the chamber height (Eq. 1),

$$F_i = H \cdot \frac{dC_i}{dt} \quad (1)$$

164 where H (m) is the overlying water height in the benthic chamber, C_i represents the concentration of
165 the analyte i (TA or DIC, in mmol m^{-3}), and t is time (d).

166

167 *2.4 In situ microprofiling of dissolved oxygen and pH*

168 A separate benthic lander, carrying a benthic microprofiler (Unisense®), was deployed to
169 measure *in situ* microprofiles of dissolved oxygen and pH (Cai and Reimers, 1993; Rabouille et al.,
170 2003, Rassmann et al., 2016 and references therein). Up to five oxygen and two pH microelectrodes
171 were simultaneously deployed, and vertical depth profiles were measured with a 200 µm resolution.
172 As their response to variations in oxygen concentrations is linear, the O_2 microelectrodes (Boudreau

and Jorgensen, 2001) were calibrated with a two-point calibration technique using the bottom water O_2 concentration determined by Winkler titration and the anoxic pore waters. The pH microelectrodes were calibrated using NBS buffers (pH 4.00, 7.00, and 9.00 at 20°C) and the spectrophotometrically determined pH of the bottom waters was used to correct for the difference in the liquid junction potential between seawater and the NBS buffers. Signal drift of O_2 and pH microelectrodes during profiling was checked to be less than 5 %.

2.5 Sediment sampling, porosity measurements, and ex situ voltammetric profiling

At each sampling station, six sediment cores (2 for pore waters, 1 for porosity, 1 for voltammetry, 1 for methane, and 1 for archives) were collected using an UWITEC® single corer (length 60 cm, inner diameter 9 cm) within 30 m from the site where the landers were deployed and processed within 30 minutes after collection. Sediment porosity profiles were determined by slicing one of the cores with a 2 mm resolution until 10 mm depth, a 5 mm resolution until 60 mm, and a 10 mm resolution down to the bottom of the cores. Porosity was calculated from the bottom water salinity, an average sediment density of 2.5 g cm^{-3}, and the weight difference between the wet and dried sediment after one week at 60 °C.

Ex situ voltammetric profiles were obtained in a separate core with a AIS, Inc. DLK-70 potentiostat in a three electrode configuration, including Hg/Au working microelectrode constructed from Pyrex glass pulled to a tip of 0.4 mm diameter to minimize particle entrainment during the profiles (Luther et al., 2008), an Ag/AgCl reference electrode, and a platinum counter electrode. The Hg/Au voltammetric electrode was deployed in the sediment using a DLK MAN-1 micromanipulator (AIS, Inc). Using a combination of linear sweep and anodic and cathodic square wave voltammetry, Hg/Au voltammetric microelectrodes are able to simultaneous quantify dissolved O_2, Mn^{2+}, Fe^{2+}, total dissolved sulfide (including elemental sulfur and polysulfides which cannot be easily distinguished from reduced sulphide; $\Sigma H_2S = H_2S + HS^- + S^0 + S_x^{2-}$), as well as organic complexes of Fe(III) (org-Fe(III)) and iron sulfide clusters (FeS_{aq}), which are not

quantifiable but reported in normalized current intensities (Tercier-Waeber and Taillefert, 2008). Hg/Au microelectrodes were calibrated for dissolved O_2 using *in situ* temperature and salinity of the overlying waters to determine the dissolved O_2 concentrations at saturation (Luther et al., 2008). They were also calibrated externally with $MnCl_2$ to quantify all other species according to the pilot ion method (Luther et al., 2008). All voltammetric data was integrated using VOLTINT, a semi-automated Matlab® script with peak recognition software (Bristow and Taillefert, 2008).

2.6 Pore water and solid phase extractions and analyses

Between 12 and 15 ml of sediment pore waters at each sampled depth were extracted from a third sediment core using rhizon filters with a mean pore size of 0.1 µm (Seeberg-Elverfeldt et al., 2005) in a glove bag that was extensively flushed with N_2 to create an anaerobic atmosphere (monitored with an O_2 sensor and verified with a 2 % ($(NH_4)_2$ $Fe(SO_4)_2$ $\cdot 6H_2O$) solution). Pore waters were subsampled within 2 hours onboard. A sample volume of 1 ml was immediately used for dissolved phosphate analysis using the paramolybdate method (Murphy and Riley, 1962) as well as for dissolved Fe^{2+} and total dissolved iron analysis using the ferrozine method (Stookey, 1970). Pore water and bottom water fractions were poisoned with $HgCl_2$ for TA and DIC or acidified to pH 1 with ultrapure HCl for sulfate and stored at 4 °C until analysis in the laboratory. Total alkalinity was measured on 3 - 6 ml sample volume by open cell titration with 0.01 M HCl (Dickson et al., 2007). Depending on the available sample volume, duplicate or triplicate titrations were performed. DIC concentrations were analyzed with a DIC analyzer (Apollo/SciTech®) on 1 ml samples as previously described (Rassmann et al., 2016) and reported as the average and standard deviations of triplicate measurements. The TA and DIC methods were calibrated using certified reference materials for oceanic CO_2 measurements provided by the Scripps Institution of Oceanography (batch n°136). The relative uncertainty for both DIC and TA was ± 0.5 % of the final value. Sulfate concentrations were quantified on 100 µl sample volumes after dilution by ion chromatography on an ICS 1000 chromatograph (Dionex) with an IonPac AS 9 HC column and AG 9 HC guard by

suppressed conductivity with an AERS 500 suppressor (ThermoFisher Scientific). A 9 mM solution of Na_2CO_3, at a flow rate of 1 ml min^{-1} was used as the eluent. The relative uncertainty of this method was ± 1.6 %. To validate a newly developed high performance liquid chromatography method (Beckler et al., 2014), pore water fractions from a separate core were also frozen at -18 °C for sulfate analysis back in the laboratory. For this new method, a Waters, Inc. 1525 binary pump with Waters 2487 absorbance detector at 215 nm was used with a Metrohm Metrosep A Supp 5 anion exchange column (150 mm x 4.0 mm) with a 1.0 mM $NaHCO_3$ / 3.2 mM Na_2CO_3 eluent at a flow rate of 0.7 ml min^{-1} (Beckler et al., 2014). To measure ammonium (NH_4^+) concentrations, 1 ml subsamples were diluted and analysed using the indophenol blue method (Grasshof et al., 1983). The uncertainty of the method was about 5 %. Pore water fractions of 1 ml volume were also acidified with 2 % HCl for Ca^{2+} analysis by inductively-coupled plasma atomic emission spectroscopy (Ultima 2, Horiba Scientific). The method was validated with mono-elemental standards and standard solutions (IAPSO, CASS-4, and NASS-6 seawater reference materials) and displayed an external relative uncertainty of ± 2-3 % depending on the sample series and a detection limit of 100 µmol l^{-1}.

Close to the Rhône River mouth, at station A, Z, and AK, one additional core was subsampled for methane analysis with 1 cm diameter corers made of cut 10-ml syringes inserted every 5 cm through pre-drilled holes on the side of the core. Due to the technical challenge of sampling non soluble methane in pore waters, this sampling could not be carried out on the same cores as the other pore water analyses. The content of these subsamples was carefully inserted in gas tight vials containing deionized water and $HgCl_2$ solution and kept at 4°C until methane analysis. Dissolved methane was quantified after degassing of the pore waters into the headspace and quantified by gas chromatography with a relative uncertainty of ± 5 % (Sarradin and Caprais, 1996). The position of the sulfate-methane transition zone (SMTZ) was determined as the zone around the depth where $[SO_4^{2-}] = [CH_4]$ (Komada et al., 2016). Finally, acid volatile sulfur (AVS) for the determination of FeS_s was extracted from the same sediment used for the pore water extractions after slicing into

layers of 1 to 5 cm. FeS_s measurements were conducted in triplicate by cold acid distillation of H_2S (g) under anoxic conditions that was trapped by NaOH and quantified voltammetrically (Henneke et al., 1991).

2.7 Nanoparticulate FeS and ion activity product for FeS precipitation

As a significant fraction of FeS nanoparticles may pass through the rhizon filters (0.1µm) used to extract pore waters (Nakayama et al., 2016) and the ferrozine method is well known to dissolve FeS nanoparticles (Davison et al., 1998), the difference between spectrophotometrically-determined Fe^{2+} concentrations ($[\Sigma Fe^{2+}]_{FR}$) and electrochemically-determined Fe^{2+} concentrations ($[Fe^{2+}{}_{echem}]$) in the pore waters was attributed to FeS nanoparticles (FeS_0), as demonstrated previously (Bura-Nakic et al., 2009; Eq. 2).

$$[FeS_0] = [\sum Fe^{2+}]_{FR} - [Fe^{2+}_{echem}] \quad (2)$$

In this interpretation, FeS_0 nanoparticles encompass both the molecular clusters of FeS (FeS_{aq}) detected electrochemically, which must be smaller than 5 nm in diameter to diffuse to the electrode (Buffle, 1988), and the larger FeS nanoparticles that are not detected voltammetrically. As electrochemically measured $FeS_{(aq)}$ cannot be quantified, both FeS forms can unfortunately not be compared directly.

2.8 Calculations of oxygen uptake and AVS burial rates

Diffusive oxygen uptake (DOU) rates were calculated using Fick's first law (Berner, 1980, Eq. 3),

$$DOU = -\emptyset \cdot D_s \cdot \frac{d[O_2]}{dz}\Big|_{z=0} \quad (3)$$

where ϕ is the dimensionless sediment porosity, D_s is the apparent diffusion coefficient in the sediments ($cm^2\ s^{-1}$), and $\frac{d[O_2]}{dz}\Big|_{z=0}$ is the oxygen gradient below the SWI (µmol mm^{-1}). For the calculations, the gradient from 0 to 400 µm in the sediment was used. The D_s coefficients were

adjusted for diffusion in a porous environment according to: $D_s = \frac{D_0}{(1+3\cdot(1-\emptyset))}$ with the diffusion coefficient in free water (D_0) taken from Broecker and Peng (1974) and recalculated at *in situ* temperature by the Stokes-Einstein relation (Li and Gregory, 1974).

AVS burial fluxes were estimated using available sedimentation rates (Charmasson et al., 1998; Miralles et al., 2005), average AVS concentrations and porosities of each sediment core, according to Eq. 4,

$$AVS_{burial} = (1 - \emptyset) \cdot \omega \cdot AVS \cdot \rho \quad (4)$$

where ω the sedimentation rate (cm yr^{-1}) and ρ the sediment dry bulk density (g cm^{-3}).

2.9 Stoichiometric ratios

Anaerobic mineralization of organic matter follows various complex reaction pathways (Table 1), but the relationships between key concentrations help understand which processes are dominant (Burdige and Komada, 2011). To determine the relationship between net TA and DIC production and to establish whether sulfate reduction represents the main source of TA and DIC in these sediments, stoichiometric ratios of the relative production of TA compared to DIC (r_{AD}), as well as TA (r_{AS}) and DIC (r_{DS}) compared to sulfate consumption, were calculated from the pore water data and compared to theoretical ratios from the reaction stoichiometries (Table 1). These ratios are equivalent to slopes in DIC-TA diagrams that can be used to identify the dominant processes controlling the carbonate system (Pain et al., 2019). For each station, experimental stoichiometric ratios were obtained from the slope and standard deviation of the linear regression of ΔTA, ΔDIC, and ΔSO_4^{2-} property-property plots. The Δ_i values represent concentration changes with respect to bottom water concentrations for component i and were corrected by multiplying their values by their diffusion coefficient (Δ_i * D_i; Berner, 1980), where D_i is the sediment diffusion coefficient for component i. The corresponding diffusion coefficients corrected for temperature and salinity (cm^2 s^{-1}) were adopted from Li and Gregory (1974). At the pH of pore waters (pH_T ~ 7.5 at 20°C, S =

38.0), more than 95% of DIC and carbonate alkalinity are composed of bicarbonate ion (HCO_3^-). Given the relatively small difference in the diffusion coefficients of HCO_3^- and CO_3^{2-} (11.8 and 9.55 x 10^{-6} cm^2 s^{-1} at 25°C, Li and Gregory, 1974) and the high proportion of HCO_3^- relative to CO_3^{2-}, the diffusion coefficient of HCO_3^- was adopted for both TA and DIC diffusion.

As calcium carbonate precipitation occurs in the sediments of the Rhône River delta (Rassmann et al., 2016), the effect of $CaCO_3$ precipitation on TA and DIC variations was also accounted for by considering the Ca^{2+} concentration gradients in the pore waters. We assumed that the stoichiometric ratio of $CaCO_3$ represents a good approximation as more than 95 % of the calcium carbonates in this area are composed of calcite (Rassmann et al., 2016). For these calculations, the absolute value of measured ΔCa^{2+}, i.e. Ca^{2+} concentration relative to its bottom water concentration, was added to the ΔTA or ΔDIC after taking the corresponding diffusion coefficients into account ($D_{TA*}\Delta TA + 2D_{Ca}*|\Delta Ca^{2+}|$ for alkalinity and $D_{DIC*}\Delta$ DIC + $D_{Ca*}|\Delta Ca^{2+}|$ for DIC) and plotted against $D_{SO42-*}\Delta SO_4^{2-}$. The calculated slope provided a stoichiometric ratio corrected for the precipitation of calcium carbonate (r_{IJc}). Pore water saturation states with respect to calcite (Ω_{Ca}) were calculated according to the equation proposed by Mucci (1983) and Millero (1983, 1995). Theoretically, organic alkalinity has to be considered in the calculation of r_{AD} and r_{AS} ratios, however, this study does not contain enough data to access organic alkalinity properly and the expected effect of organic alkalinity on these ratios was low (section 4.2).

3. Results

3.1 Bottom water and surface sediment characteristics

At all stations, bottom water salinity ranged from 37.5 to 38.0 and temperature varied from 14.7 to 20.6 °C (Table 2). Average TA (2.60 ± 0.01 mM) and DIC (2.30 ± 0.02 mM) concentrations (Table 2) were relatively high compared to the Mediterranean Sea, but common for the Gulf of Lions (Cossarini et al., 2015). The pH_T of the bottom waters varied from 8.05 to 8.09 with the

317 highest value observed at station AK and the lowest at station E. Although the oxygen concentration
318 decreased with water depth, bottom waters were always well ventilated, with dissolved O_2
319 concentrations higher than 220 µmol L^{-1}. Sediment porosity ranged between 0.7 and 0.8 at the SWI,
320 and they were similar at all stations between 20 and 400 mm depth (Table 2).

321 *3.2 Benthic total and diffusive fluxes*

322 The *in situ* pH and O_2 microprofiles reflected the differences between the three study domains
323 under the influence of the Rhône River plume (Fig. 2). In the proximal zone (stations A and Z), the
324 oxygen penetration depth (OPD) was only 1.5 to 2.5 mm into the sediment as also indicated by
325 separate microprofile measurements (Fig. 2). The OPD increased from 2 to 6 mm at station K and
326 reached 8 to 11 mm at the most offshore station E. As a result of bad weather conditions, no
327 exploitable *in situ* microprofiles were recorded at stations AK and B, though *ex situ* voltammetric
328 profiles determined oxygen penetration depths of 4 and 2 mm, respectively (Fig. 4). All pH
329 microprofiles indicated a pH minimum between 7.2 and 7.4 just below the OPD followed by an
330 increase to between 7.5 and 7.6 in the manganese/ferruginous layers of the sediment around 5 mm
331 inshore and below 12 mm offshore (Fig. 2). Below this depth, the pH stabilized in the pore waters.
332 The benthic chamber was deployed once at stations A and E and twice at station Z (Z' is the
333 replicate). Total alkalinity and DIC concentrations increased linearly with time (10 to 22 hrs) in the
334 chamber (Fig. S1), but concentration changes decreased along the nearshore-offshore transect.
335 Minimal disturbance of the sediment-water interface during deployments was evidenced by the
336 initial DIC and TA concentrations which were within 5% and 8% respectively of the bottom water
337 concentration (Fig. S1). The highest benthic fluxes were recorded for the two deployments at station
338 Z, with TA fluxes of 73.9 ± 20.6 and 56.0 ± 17.8 mmol m^{-2} d^{-1} and DIC fluxes of 78.3 ± 10.9 and
339 37.2 ± 7.2 mmol m^{-2} d^{-1} (Fig. 3, Table 2). The relatively high variability between these two
340 measurements is probably due to high spatial heterogeneity of the sediments due to the deposition
341 conditions during floods. At station A, the benthic TA and DIC fluxes reached lower values of 14.3

± 1.6 and 17.8 ± 1.6 mmol m^{-2} d^{-1}, respectively, while benthic fluxes were lowest at station E, with a TA flux of 3.7 ± 0.9 mmol m^{-2} d^{-1} and a DIC flux of 9.9 ± 0.9 mmol m^{-2} d^{-1}. In parallel, DOU rates reached 10.2 ± 1.3 and 10.4 ± 0.9 mmol m^{-2} d^{-1} at stations A and Z and decreased offshore to 5.9 ± 1.0 mmol m^{-2} d^{-1} at station K and 3.6 ± 0.6 mmol m^{-2} d^{-1} at station E (Fig. 3, Table 2). Although DOU rates and DIC fluxes tend to converge offshore, the TA and DIC fluxes in the proximal zone were between 2 and 8 times larger than the absolute value of the DOU rates (Fig. 3). In this area, DOU rates are quite representative of total oxygen uptake (TOU) by the sediments as TOU:DOU ratios are typically around 1.2 +/- 0.4 (Lansard et al., 2009).

3.3 Electrochemistry profiles

Dissolved Fe^{2+} concentrations as a function of depth in the sediment mirrored the voltammetric signals of soluble organic-Fe(III) complexes at stations A, Z, AK, B, and K (Fig. 4). High concentrations of dissolved Fe^{2+} were observed in the proximal domain at stations A (maximum of 341 ± 22 µM) and Z (maximum of 234 ± 25 µM), where dissolved ΣH_2S was not detected (Fig. 4). At station AK, the shallowest station in the prodelta domain, dissolved Fe^{2+} increased to a maximum concentration of 255 µM around 2 cm depth, then decreased with sediment depth as FeS_{aq} below 6.5 cm and small concentrations of dissolved ΣH_2S around 17 cm were produced (Fig. 4). The two deeper prodelta stations, B and K, displayed lower Fe^{2+} concentrations, including one peak not exceeding 81 µM (station B) or 73 µM (station K) in the top 2 cm of the sediment and a second peak not exceeding 50 µM between 12-14 cm (station B) and 86 µM between 5-7.5 cm (station K) in the sediment. Although FeS_{aq} was only detected below 15 cm at station K, ΣH_2S was produced in low concentrations (< 5 µM) around 6.5 cm at stations B and K (Fig. 4). A peak of Fe^{2+} was initially formed in the top 5 cm of the distal domain (station E) but decreased to a minimum value with depth and did not correlate with the organic-Fe(III) voltammetric signals, which also remained low throughout the profile (Fig. 4). Finally, station E displayed generally low concentrations of ΣH_2S in the pore waters (< 6 µM), though the onset of ΣH_2S production was

much shallower (2.5 cm) and ΣH_2S concentrations were consistently higher throughout the profile than at any other station.

3.4 Geochemical characteristics of the pore waters and sediments

In general, the pore water geochemical composition of duplicate cores collected at each station matched well, except at stations A and Z where some variations in TA, DIC, and sulfate concentrations provide evidence for the heterogeneity of deposition processes in the proximal domain (Fig. 5). Both TA and DIC concentrations increased rapidly within the pore waters, likely reflecting the intensity of organic carbon mineralization rates in these sediments. At all stations, DIC pore water concentrations correlated well with TA (overall slope: 1.01 ± 0.006, r^2=0.995, n=134). The TA and DIC gradients were highest at stations A and Z, where maximum concentrations of both species reached around 55 mM (Fig. 5). At station AK, TA and DIC concentrations reached a maximum of 15 mM at 25 cm depth but decreased to 6 mM at the bottom of the core. The maximum concentrations of TA and DIC of 35 mM observed at station B, were more comparable to the stations in the vicinity of the river mouth (stations A and Z) than other stations located in the prodelta domain (stations AK and K). At station K, TA and DIC concentrations reached 10 mM, whereas the lowest TA and DIC gradients were measured at station E, with concentrations reaching only 4.6 mM at the bottom of the cores (30 cm). Sulfate was completely removed from the pore waters at depths of 35, 24, and 45 cm at station A, Z, and B, respectively (Fig. 5). In turn, sulfate concentrations decreased to a minimum concentration of 20 mM at 29 and 24 cm depth at stations AK and K, whereas sulfate consumption was much smaller at station E with a minimum concentration of 28 mM (bottom water sulfate concentration was 31.4 mM). As a result, TA and DIC changes in concentration at a given depth were highly inversely correlated ($r^2 > 0.98$) with sulfate changes in concentration at stations A, Z, AK, B, and K (Table 3). At station E, sulfate variations with depth were limited and the uncertainty on ΔSO_4^{2-} was too large to calculate r_{AS} and r_{DS}. TA and DIC demonstrated strong correlations ($r^2 > 0.97$) at stations A, Z,

AK, B, and K (Table 3). In the proximal domain (stations A and Z), ammonium increased with sediment depth to concentrations > 3 mM (Fig. 5). At station B, ammonium reached concentrations > 2 mM with depth, whereas ammonium concentrations did not exceed 1.5 mM at station AK, 0.6 mM at station K, and 0.3 mM at station E. Even though individual pore water profiles from replicate sampling (pore waters from two different cores were sampled and analyzed for DIC, TA, and SO_4^{2-} at each station) were slightly different at some stations, the r_{AD} and r_{AS} and r_{DS} ratios were the same. At all stations, nitrite plus nitrate concentrations were less than 20 µM (data not shown). Significant methane concentrations (> 50 µM) were detected at the bottom of the sediment core at stations A, Z, and AK (Fig. 5), and a SMTZ was tentatively identified between 28 and 39 cm at station A and between 19 and 39 cm at station Z as the use of pore water data from different cores is not straightforward given the high heterogeneity of sediment deposits in the proximal domain. As methane was < 50 µM throughout the profile at station K and sulfate was not completely consumed inside the sediment core at station AK, the SMTZ was not determined at these two stations. Methane analyses were not carried out for the other stations.

The sediment pore waters were supersaturated with respect to calcite (Ω_{Ca} > 1) at all stations and supersaturated with respect to aragonite except for the surface at stations B and K. At stations A, Z, and B, decreasing Ca^{2+} concentrations in the pore waters indicated precipitation of $CaCO_3$, whereas Ca^{2+} concentrations remained close to the bottom water Ca^{2+} concentrations (11.2 mM in Mediterranean waters) at the other stations (Fig. 5). Dissolved phosphate concentrations (ΣPO_4^{3-}) were relatively high (50-100 µM) throughout the profiles at stations A, AK, K and Z, and a large increase in concentration (up to 160 µM at station Z) was observed at station AK, K and Z between 15 and 22 cm. In turn, ΣPO_4^{3-} production was minimal in station E pore waters (< 10 µM). Dissolved phosphate was not measured at station B. Sediment samples were analyzed for AVS as a function of depth at stations A, AK, and E to assess one station in each domain (Fig. 5). At station A, a peak in AVS (65 µmol g^{-1}) was measured around 8.0 cm followed by a second, smaller peak (22 µmol g^{-1}) at 14 cm, after which AVS decreased with depth. The AVS concentrations were low

418 in the top portion of the sediment at station AK but increased with depth to 100 µmol g^{-1} around 15
419 cm. At station E, only a small AVS peak of 20 µmol g^{-1} was observed at 14 cm. Finally, large
420 concentrations of FeS nanoparticles (FeS_0) were found in the proximal and prodelta stations,
421 including two broad peaks and maximum concentrations around 1 mM at stations A and Z and a
422 large subsurface maximum up to 6 mM at 145 mm at station AK. These FeS_0 concentrations
423 increased as a function of depth to a relatively constant 0.5 mM below 4.5 cm at station B and
424 below 12 cm at station K, whereas they remained mostly negligible at station E (Fig. 5).

425 **4. Discussion**

426 The main objectives of this study were to determine the magnitude of the alkalinity source from
427 deltaic regions sediments exposed to large riverine inputs and to identify the biogeochemical
428 processes responsible for the observed benthic TA and DIC net production. In this section, benthic
429 TA and DIC fluxes in the Rhône River prodelta are first compared to other similar systems. In the
430 following sections, the most likely biogeochemical processes responsible for the high benthic TA
431 fluxes are identified based on the sediment depth profiles collected. As calcium carbonate
432 dissolution, denitrification, and organic alkalinity can be discarded as major TA sources from these
433 sediments (see discussion below), the role of iron sulfide mineral precipitation on the benthic TA
434 flux is examined using a variety of analytical techniques, speciation calculations, and a mass
435 balance approach. Finally, the link between inputs to the sediment, carbon mineralization processes,
436 sulfide mineral burial, and the benthic TA flux is provided using a conceptual model.
437

438 *4.1 DIC and alkalinity fluxes from the sediment*

439 The sediments of the Rhône proximal and prodelta zones represent important sources of both
440 DIC and TA to the bottom waters (Fig. 3). The observed fluxes show some variability between
441 stations in the proximal zone, most probably due to the high inter- (i.e., km scale between stations A

and Z) and intra-station (i.e., < 100 m between Z and Z') biogeochemical heterogeneities associated with massive and rapid deposition events during floods. This heterogeneity is also visible in pore water profiles from two different cores at station Z or A (Fig. 5). Despite this sub-kilometre variability near the river mouth, the biogeochemical gradient from the proximal zone to the continental shelf is large enough to contrast the different zones. The DIC fluxes observed in the proximal domain (18-78 mmol m^{-2} d^{-1} at station A and Z; Fig. 3) are in the range of previously measured fluxes in other deltas where anaerobic mineralization processes are dominant, including Mississippi delta sediments from core incubations (15-20 mmol m^{-2} d^{-1}; Lehrter et al., 2012) or benthic chambers (36-53 mmol m^{-2} d^{-1}; Rowe et al., 2002), benthic chamber measurements in Po River delta sediments and the Adriatic shelf (15-25 mmol m^{-2} d^{-1}; Hammond et al., 1999), the Fly River delta during the most active season (35-42 mmol m^{-2} d^{-1}; Aller et al., 2008) and near the Guadalquivir River estuary (36-46 mmol m^{-2} d^{-1}; Ferron et al., 2009). In contrast, fewer alkalinity fluxes were measured in river deltas, though those obtained from benthic chambers in the Danube and Dniester deltas in the Northwest Black Sea (21-67 mmol m^{-2} d^{-1}; Friedl et al., 1998), are within the range of values reported in this study (14-74 mmol m^{-2} d^{-1}). Benthic TA fluxes obtained in the Guadalquivir estuary (24-30 mmol m^{-2} d^{-1}; Ferron et al., 2009) and the Adriatic shelf sediments off the Po River delta (0.5-10.4 mmol m^{-2} d^{-1}; Hammond et al., 1999) are in the lower range of TA fluxes measured in the present study, likely because the sampling stations were located further on the shelf. The biogeochemical origin of these TA benthic fluxes is discussed in the next sections.

4.2 Production of alkalinity by calcium carbonate dissolution and denitrification in coastal marine sediments

Calcium carbonate dissolution, denitrification from imported nitrate, and burial of FeS or FeS_2 following iron hydroxide and sulfate reduction produce significant alkalinity in coastal marine sediments that may be transferred to the overlying waters (Hu et Cai, 2011a). In this section we examine if the first two processes contribute to the observed TA fluxes in the Rhone delta area.

467 Calcium carbonate dissolution may occur immediately below the SWI as a result of the acidity
468 generated by aerobic respiration, and may thus represent a possible contributor to TA fluxes as
469 demonstrated in carbonate-rich permeable sediments (e.g., Burdige and Zimmerman, 2002;
470 Cyronak et al., 2013; Rao et al., 2014). As about 95 % of the $CaCO_3$ minerals in this area are made
471 of calcite (Rassmann et al., 2016), the discussion is focussed on this phase, but the calculations have
472 also been made for aragonite. In the proximal zone, both the water column ($\Omega_{Ca} = 5.5$) and the pore
473 waters at depth ($\Omega_{Ca} > 1$) are largely supersaturated with respect to calcite and aragonite (Rassmann
474 et al., 2016; Fig. 5) suggesting that carbonate mineral dissolution is not significant. These findings
475 are corroborated by a large decrease in Ca^{2+} concentration in the pore waters, indicating instead
476 $CaCO_3$ precipitation at depth in proximal zone sediments. Yet, the large pH decrease in the first
477 millimeters below the sediment-water interface (Fig. 2) may induce carbonate dissolution at this
478 scale. Calcium carbonate saturation states at a millimeter scale near the SWI were calculated from
479 pH profiles and interpolation of the centimetre-scale DIC profiles using the Seacarb software (Fig.
480 6). These calculations show that in the proximal zone, the saturation state with respect to calcite is
481 always above 1.5 and always above 1 for aragonite. Such saturation state precludes massive
482 carbonate dissolution at the sediment surface and discounts shallow carbonate dissolution as playing
483 a large role on the benthic alkalinity fluxes observed in proximal sediments. Minor quantities of
484 calcium carbonate or magnesian calcite may be dissolved in microniches where the pH could be
485 lower than 7.4. These processes, however, do not visibly imprint the Ca^{2+} profile (Fig. 5) and
486 surely represent an insignificant fraction of the large TA benthic flux measured in the proximal
487 zone. At the distal shelf station (Station E, Fig. 6c), the saturation state was close to 1 for calcite and
488 slightly undersaturated for aragonite which may indicate a potential contribution of calcium
489 carbonate dissolution to the benthic alkalinity flux in this area.
490 As coupled nitrification-denitrification is neutral to TA net production, denitrification based on
491 an external source of nitrate represents the second potential net source of TA in marine sediments
492 (Hu and Cai, 2011b). In the Rhône prodelta, the stratification of the water column prevents large

493 inputs of riverine nitrate to bottom waters as evidenced by their high salinity (Table 2) and low
494 nitrate concentrations ($[NO_3^-]$= 1.5 µmol l^{-1}; Bonin et al., 2002). Furthermore, nitrate profiles in
495 pore waters generally display a subsurface peak indicating nitrate efflux which also prevents
496 benthic denitrification of bottom water nitrate (Pastor et al., 2011). It can therefore be concluded
497 that the contribution of denitrification to TA fluxes is minimal in the sediments of the Rhône River
498 delta.
499 In the bottom waters, organic alkalinity was estimated from TA, pH and DIC concentrations to
500 represent less than 1% of TA. In the pore waters, the data set did not allow estimating organic
501 alkalinity directly, but the r_{AD} close to 1 indicates that the organic alkalinity fraction is limited
502 contrarily to previous findings where organic alkalinity plays an important role and r_{AD} ratios > 1.3
503 have been recorded at similar pH (Lukawska-Matuszewska, 2016).
504 In the next sections, we detail the last process producing alkalinity, i.e. FeS production and burial.

505 *4.3 DIC and TA produced by sulfate reduction*

506 Sulfate reduction typically represents a major organic carbon mineralization pathway in
507 organic-rich sediments that simultaneously produces two moles of TA and two moles of DIC per
508 mole of sulfate reduced (Table 1, Eq. 6) (Canfield et al., 1993b; Burdige, 2011). Dissimilatory iron
509 reduction (Table 1, Eq. 7) in turn produces 1/4 moles of DIC (HCO_3^-) and consumes 7/4 moles of
510 H^+, resulting in two moles of TA produced per mole of Fe. As these two processes equally produce
511 two moles of TA per mole of terminal electron acceptor (Table 1, Eq.6 for SO_4^{2-} and Eq. 7 for
512 $Fe(OH)_3$), they can both contribute significantly to the bulk alkalinity production in sediment pore
513 waters. The low concentration of nitrate, relatively low production of reduced metals in the pore
514 waters (Fig. 4), and intense ammonium and DIC production in parallel with sulfate consumption at
515 depth (Fig. 5) confirm that sulfate reduction is one of the dominant mineralization pathways in the
516 Rhône River prodelta sediments (Pastor et al., 2011; Rassmann et al., 2016). Assuming that sulfate
517 reduction is responsible for the majority of the bulk alkalinity production, experimentally-derived

stoichiometric ratios of the relative production of DIC and TA compared to sulfate consumption may identify the effect of other reaction pathways responsible for bulk alkalinity production or consumption in these sediments (Burdige and Komada, 2011). Factoring carbonate precipitation using pore water Ca^{2+} data, the r_{DSc} ranged between -2.05 and -1.86, except for one value at -1.37 (station B), whereas the r_{ASc} ratios ranged between -2.35 and -1.89 with the exception of station B at -1.58 (Table 3). Theoretically, the r_{DS} and r_{AS} should equal -2.0 if sulfate reduction is the only control on DIC and TA production (Table 1, Eq. 6), suggesting that, except at station B, the influence of other diagenetic processes on r_{ASc} and r_{DSc} is limited. At station B, however the higher r_{DSc} ratio (Table 3) may indicate significant anaerobic oxidation of methane (AOM Table 1, Eq. 8) which generates a theoretical r_{DS} of -1 (Borowsi et al., 1996; Komada et al., 2016). Unfortunately, methane sampling was not performed at station B, preventing precise identification of AOM at this station.

4.4 Formation of iron sulfide species

Although the complete depletion of sulfate in the first 30 cm of the sediment at stations A, Z, and B implies an equivalent production of dissolved sulfide (ΣH_2S) (Table 1, Eq. 6), pore waters displayed little to no ΣH_2S (Fig. 4). If all of the produced ΣH_2S diffused upward and reacted in the oxic sediment layers, the alkalinity produced by sulfate reduction would be consumed by the oxidation of ΣH_2S by dissolved O_2 and the pH should be lowered significantly given the large acidity generated by this reaction (Table 1, Eq. 4). Although ΣH_2S was nearly absent of the pore waters (Fig. 4), the pH minimum was never lower than 7.2 and the observed alkalinity fluxes across the SWI were substantial (Fig. 3), indicating that ΣH_2S was removed from the pore waters below the oxic layer. Abiotic reduction of Fe(III) oxides by ΣH_2S (Table 1, Eq. 9), followed by precipitation of FeS in the anoxic zone (Table 1, Eq. 10; Berner, 1970; Pyzik and Sommer, 1981; Carman and Rahm, 1997, Soetaert et al., 2007), and eventually formation of pyrite (Table 1, Eq. 11; Rickard and Luther, 1997) may represent a significant ΣH_2S removal pathway. As the precipitation

543 of siderite is too slow to compete with FeS precipitation (Jiang and Tosca, 2019; Pyzik and
544 Sommer, 1981) and the abiotic reduction of Fe(III) oxides by ΣH_2S coupled with either FeS or FeS
545 and pyrite precipitation (Table 1, Eq. 9-11) does overall not alter alkalinity, bacterial sulfate
546 reduction followed by abiotic precipitation of iron and sulfide from the pore waters to either FeS or
547 pyrite (Table 1, Eqs. 12 and 13) should result in $r_{AD} = 1$ and $r_{DS} = r_{AS} = -2$. Formation of pyrite is
548 accompanied by the consumption of molecular H_2 by sulfate-reducing bacteria, resulting in a slight
549 increase in the r_{AD} and r_{DS} to 1.1 and -1.81 for the overall reaction while the r_{AS} ratio should not
550 change (Table 1, Eq. 14).

551 The observed range of r_{ADc} (1.06 to 1.15) and r_{DSc} (-2.05 to -1.86) ratios in the proximal and
552 prodelta stations, except at station B (Table 3), is fully compatible with sulfate reduction coupled to
553 iron reduction and FeS precipitation (possibly followed by pyritization), though r_{ADc} and r_{DSc} ratios
554 are not able to distinguish abiotic and microbial pathways of iron reduction. Indeed, the
555 concomitant production of Fe^{2+} by dissimilatory iron reduction (Table 1, Eq. 7) and ΣH_2S by sulfate
556 reduction followed by precipitation of FeS decreases the net r_{AD} and r_{DS} ratios to 0.89 and -2.25,
557 whereas the r_{AS} ratio remains at -2 (Table 1, Eq. 15). With ensuing formation of pyrite, theoretical
558 mole ratios change slightly to $r_{AD} = 0.94$ and $r_{DS} = -2.13$ without H_2 reoxidation (Table 1, Eq. 16) or
559 1.06 and -1.89 with H_2 reoxidation (Table 1, Eq. 17). The occurrence of dissimilatory iron reduction
560 in the proximal and prodelta domains, however, is substantiated by several other pieces of evidence.
561 First, the production of soluble organic-Fe(III) complexes deeper than the oxygen penetration
562 depths (Fig. 4) indicates that these species did not result from the oxidation of Fe^{2+} by dissolved O_2
563 in the presence of organic ligands (Taillefert et al., 2000). Second, as soluble organic-Fe(III)
564 complexes are produced as intermediates in the reduction of Fe(III) oxides by iron reducing bacteria
565 (Taillefert et al., 2007; Jones et al., 2010), their concomitant detection with Fe^{2+} at all stations in the
566 proximal and prodelta domains (Fig. 4) suggests they were produced during dissimilatory iron
567 reduction. Third, the positive correlation between the current intensities of organic-Fe(III)
568 complexes and Fe^{2+} concentrations is in line with the same correlation obtained in iron-rich deep-

sea sediments (Fig. 7) where sulfate reduction was not significant (Beckler et al., 2016). Finally, as these organic-Fe(III) complexes are readily reduced by ΣH_2S (Taillefert et al., 2000), their presence in zones of sulfate reduction suggests these sediments are biogeochemically dynamic with periods of microbial iron reduction followed by sulfate reduction and rapid FeS precipitation which culminates in spring and summer. This dynamics may be temporally initiated by the input of organic and inorganic material from the Rhône River in the proximal domain during major floods in late fall and winter, which generates, during spring and summer, large DIC and TA concentrations, large iron(II) concentrations, and completely exhaust sulfate at depth in the pore waters (Pastor et al., 2018) in a reproducible manner over the years.

4.5 FeS precipitation

The discrepancy between sulfate consumption and the low concentration of ΣH_2S along with the high benthic TA fluxes clearly suggest that much of the sulfide was precipitated in the solid phase. Indeed, AVS measurements show precipitation of FeS in the proximal and prodelta domains (Fig. 5). In addition, the large phosphate concentrations observed at depth in the proximal and prodelta domains (Fig. 5) suggest that ΣPO_4^{3-} adsorbed to Fe(III) oxides was released in the pore waters during secondary conversion of Fe(III) oxides to FeS (Anschutz et al., 1998; Rozan et al., 2002). More importantly, large concentrations of nanoparticulate FeS (FeS_0 in the range of 1-6 mM) were identified in the proximal and prodelta stations and decreased with distance from shore (Fig. 5). The existence of FeS_0 suggests that large fractions of Fe^{2+} and ΣH_2S were actively removed from the pore waters at the time of measurements and eventually immobilized under the form of sulfide minerals. Although soluble FeS_{aq} clusters detected electrochemically when the system is supersaturated with respect to FeS (Theberge and Luther, 1997) are considered good indicators of the active precipitation of iron sulfide minerals (Luther and Ferdelman, 1993; Davison et al., 1998; Taillefert et al., 2000), they were rarely observed in the Rhône River delta (Fig. 4). Collectively, the large concentrations of FeS_0 compared to the small electrochemically active FeS_{aq} complexes,

the absence of ΣH_2S despite complete removal of sulfate along with the generally low saturation state of the pore waters with respect to FeS (Fig. S2) indicate that the proximal and some of the prodelta stations were not at equilibrium and FeS was partly aggregated during this time period.

4.6. Benthic alkalinity flux as a result of iron sulfide burial

As sediments rapidly accumulate in the proximal domain during flood events (Maillet et al., 2006; Cathalot et al., 2010; Zebracki et al., 2015), the burial of FeS becomes irreversible and thus represents a net source of alkalinity to the bottom waters (Berner, 1982; Hu and Cai, 2011a; Brenner et al., 2016). With the precipitation of FeS, about 2 to 3 moles of alkalinity equivalent should be produced for each mole of sulfur precipitated (Table 1, Eqs. 12 and 15). Assuming dissimilatory microbial iron and sulfate reduction dominate in the proximal and prodelta zones, a conservative ratio of 2 moles of TA equivalent per mole of FeS precipitated can be estimated (Table 1, Eq. 15). The calculated AVS burial flux provides an alkalinity-equivalent flux of 25.0 ± 7.7 mmol m^{-2} d^{-1} in the proximal domain (Table 4), which falls within the range of benthic alkalinity fluxes measured by benthic chamber at stations A and Z (14 - 74 mmol m^{-2} d^{-1}; Fig. 3 and Table 4). The connection between alkalinity fluxes at the sediment-water interface and FeS burial at depth is questionable given the low residence time of the sediment near the interface (< 1yr in the first 30 cm) and the temporal variability in deposition processes (see section 2.1). Chemical gradients and thus benthic fluxes are shaped by biogeochemical reactions occurring within the diffusion length, i.e. the distance (d) that can be travelled by diffusion of chemical species over a given time:

$$d = \sqrt{2 * D_S * t} \qquad (5)$$

where d is the diffusive length (cm), D_s the diffusion coefficient in the sediment (cm^2 s^{-1}) and t the time (s). For a period of 6 months (between fall and spring), and using the diffusion coefficient of HCO_3^- ($D_s = 7.10^{-6}$ cm^2 s^{-1} at 20°C), the diffusion distance reaches around 15 cm. This distance represents a minimal estimate as transport is likely enhanced by bioturbation and bioirrigation such that 20 cm of sediment and pore water may be considered connected to the SWI on a semi-annual

basis. These findings indicate that biogeochemical processes over that depth interval are able to shape net benthic alkalinity fluxes at the SWI over a 6-month period after the fall floods (Anschutz et al., 2002). The FeS burial effect is strengthened by the episodic but large deposition of new sediment during the following fall floods.

In the prodelta, the alkalinity-equivalent flux resulting from FeS burial is estimated at 9.8 ± 2.8 mmol m^{-2} d^{-1} at station AK (Table 4). This, unfortunately, cannot be compared to benthic alkalinity fluxes as they were not measured. In the distal domain, however, a low alkalinity-equivalent flux of 0.04 ± 0.1 mmol m^{-2} d^{-1} is estimated from the average FeS burial flux at station E. This flux is much lower than the 3.7 ± 0.9 mmol m^{-2} d^{-1} flux measured by benthic chamber (Fig. 3), a difference that could be due to shallow carbonate dissolution.

4.7. Linking TA and DIC fluxes to mineralization processes

Overall, the present findings indicate that FeS burial modifies the alkalinity budget in the proximal and prodelta sediments (Brenner et al., 2016). As the measured benthic alkalinity fluxes are compatible with the alkalinity generated during the reduction of Fe(III) oxides, sulfate, and subsequent FeS burial in the proximal zone, these processes are likely responsible for the large benthic alkalinity fluxes reported in this high-sedimentation delta and, potentially, other similar systems (Hu and Cai, 2011a). Although precipitation of pyrite may also preserve the bulk alkalinity generated in the pore waters, pyrite precipitation is slow enough compared to FeS precipitation (Rickard, 1995; Rickard and Luther, 1997) that it may occur only deeper in the sediment.

The biogeochemical cycling of C, Fe, S, and TA close to the Rhône River mouth can be theoretically summarized as follows (Fig. 8): (i) the high pore water DIC concentrations resulting from the production of metabolic CO_2 during organic carbon mineralization lead to benthic DIC fluxes that are only modulated by the precipitation of carbonate minerals; (ii) the high pore water TA concentrations result from intense iron and sulfate reduction as a result of the high supply of organic matter and Fe(III) oxides to the sediment and are limited by the diffusion of sulfate in the

644 sediment; (iii) the precipitation of FeS and the high sedimentation rates near the river mouth
645 preserve the majority of reduced iron and ΣH_2S buried in the form of solid FeS minerals and
646 potentially pyrite within the anoxic sediments (Aller et al., 1986); (iv) ultimately, the TA-
647 consuming reoxidation of reduced metabolites (i.e., NH_4^+, ΣH_2S, Fe^{2+}) is not important in the oxic
648 sediment layers, and a significant fraction of the anaerobically-produced TA is transferred across
649 the SWI (Fig 8, red line); and (v) benthic alkalinity fluxes may be sustained on a annual basis, as
650 the large input of sediment to the prodelta during fall floods is followed by the development of
651 anaerobic respiration processes during the spring and summer seasons. In these conditions,
652 anaerobic and aerobic processes are decoupled, and the consumption of oxygen no longer reflects
653 the overall respiration rates within these sediments (Pastor et al., 2011) as observed by the relatively
654 low DOU rates compared to TA and DIC fluxes in the proximal domain (Fig. 3).

655 In contrast, sedimentation rates (Table 2), overall respiration rates (Fig. 3), and the intensity of
656 iron and sulfate reduction (Fig. 5) decrease in the distal domain (station E), and as a consequence
657 the relative proportion of aerobic processes increases (Pastor et al., 2011). Despite the relatively
658 small decrease in pore water sulfate concentrations with depth and low ΣH_2S concentrations (< 10
659 µmol L^{-1}) at the most offshore station E, ΣH_2S concentrations were the highest of all the stations.
660 These findings likely reflect the fact that less riverine Fe(III) oxides were available for FeS
661 precipitation and that this system is probably iron limited. With low sedimentation rates (0.1 to 1
662 cm yr^{-1}) and thus low input of organic matter and Fe(III) oxides, the overall carbon turnover is
663 decreased and the reduced by-products of sulfate and/or iron reduction may be transported back to
664 the oxic sediment layers to be reoxidized by dissolved oxygen (Fig. 8). In this case, the alkalinity
665 generated by anaerobic respiration processes is consumed by reoxidation of the reduced
666 metabolites, and the flux of alkalinity near the SWI decreases to weak values at station E (Fig. 3 and
667 Fig. 8, black line).

668 The strong TA flux to the overlying waters measured in the Rhône River delta, may contribute,
669 along with riverine inputs, to the overall high alkalinity of the Gulf of Lions waters compared to the

Mediterranean average (Cossarini et al., 2015). However, the influence of the benthic TA flux on the water column pH and ultimately the absorption of atmospheric CO_2 depends mainly on the TA to DIC benthic flux ratio (F_{TA}/F_{DIC}), vertical mixing in the water column, and thus the residence time of the bottom waters (Hu and Cai, 2011b, Andersson and Mackenzie, 2012). The F_{TA}/F_{DIC} ratios, ranging between 0.8 and 1 in the proximal and prodelta zones of the Rhône River delta (Fig. 9), are in the high range of a compilation of TA to DIC flux ratios obtained in different coastal systems and continental shelves (expanded from Hu and Cai, 2011b). As these ratios do not exceed 1, alkalinity generated in the sediments will not decrease pCO_2 in the bottom waters and thus not draw significant atmospheric CO_2 into the coastal ocean. Yet, the large benthic TA fluxes generated from deltaic sediments as a result of the periodic FeS sink in these sediments after large floods will definitely impact water-column TA and carbonate system dynamics on the long term. The elevated F_{TA}/F_{DIC} ratio (>0.8), which were unknown in the Rhône River prodelta before this study, will therefore modify the carbonate cycle paradigm in these coastal regions.

5. Conclusion

Benthic alkalinity fluxes are generally attributed to the dissolution of calcium carbonate minerals or denitrification in marine sediments without thorough examination of the biogeochemical processes responsible for net alkalinity production in pore waters. In this study, benthic mineralization processes, as well as benthic alkalinity and DIC fluxes were quantified in the Rhône River delta using a combination of benthic landers and depth profiles of redox and carbonate constituents. These measurements demonstrated that sediments from the proximal and prodelta domains represent a strong source of alkalinity to the water column. The highest alkalinity and DIC fluxes were detected in the vicinity of the Rhône River mouth and were much stronger than fluxes of dissolved oxygen, indicating the decoupling of oxic and anoxic biogeochemical processes. As denitrification was not significant in these sediments and pore water supersaturation with respect to calcite prevented carbonate dissolution to occur over the entire sediment column, the high benthic

alkalinity fluxes resulted from the high intensity of sulfate reduction and precipitation of iron sulfide minerals, with contributions from dissimilatory iron reduction and AOM, modulated by the precipitation of authigenic carbonates. The high intensity of anaerobic respiration processes was likely driven by pulsed sediment accumulations during fall river floods that promoted precipitation and burial of iron sulfide minerals deep in the sediments.

Consequently, a significant fraction of the total alkalinity generated in the pore waters was transferred to the bottom waters (benthic TA fluxes ranging from 14 to 74 mmol m^{-2} d^{-1}). The intensity of the alkalinity and DIC fluxes decreased offshore as the sedimentation rate and the relative importance of anaerobic mineralization pathways compared to aerobic processes decreased. In these conditions the more "classical" coupling between aerobic and anaerobic reactions generated much lower benthic alkalinity fluxes. Overall, these findings suggest that deltaic sediments exposed to large riverine inputs of inorganic and organic material may provide a large source of alkalinity to the overlying waters and thus weaken the increase in pCO_2 more significantly than previously thought in coastal waters.

Acknowledgments

The authors thank the captain and crews of the RV Tethys II for their support at sea and Bruno Bombled for his technical help on-board and in the laboratory. We thank Gael Monvoisin for the analysis of sulfate samples at GEOPS (Paris-Sud University), Joel Craig and Olivia Studebaker for the analysis of nutrients and AVS at Georgia Tech, and Celine Liorzou for the ICP-AES measurements at Pôle Spéctrométrie Océan in Brest. The authors would also like to thank Jack Middelburg for handling the manuscript and two anonymous reviewers for their constructive comments that helped improve an earlier version of the manuscript. Finally, we are grateful to Sabine Kasten, Sandra Arndt, and Andrew Dale for interesting discussions about the interactions of AOM with carbonates and iron minerals and sediment dynamics. This research was funded by the project Mistrals/MERMEX-Rivers, the French State programme "Investissement d'avenir" ran by

721 the National Research Agency (AMORAD project ANR-11-RSNR-0002) and the National
722 Science Foundation (OCE-1438648).

723 **References**

Aller, R. C., Blair, N. E., and Brunskill, G. J. : Early diagenetic cycling, incineration, and burial of sedimentary organic carbon in the central Gulf of Papua (Papua New Guinea), J. Geophys. Res., 113, 1–22, 2008.

Aller, R. C., Mackin, J. E., and Cox, R. T. : Diagenesis of Fe and S in Amazon inner shelf muds: apparent dominance of Fe reduction and implications for the genesis of ironstones, Cont. Shelf. Res., 6, 263–289, 1986.

Andersson, A.J., Mackenzie, F.T. and Lerman, A. : Coastal ocean CO_2-carbonic acid-carbonate sediment system of the Anthropocene, Glob. Biogochem. Cycle, 20, GB1S92, 2006.

Andersson, A. and Mackenzie, F. : Revisiting four scientific debates in ocean acidification research. Biogeosci., 9, 893–905, 2012.

Anschutz, P., Zhong, S., Sundby, B., Mucci, A., and Gobeil, C.: Burial efficiency of phosphorus and the geochemistry of iron in continental margin sediments, Limnol. Oceanogr., 43, 53–64, 1998.

724 Anschutz, P., Jorissen, F.J., Chaillou, G., Abu-Zied, R. and Fontanier, C.: Recent turbidite
725 deposition in the eastern Atlantic: Early diagenesis and biotic recovery. J. Mar. Res, 60, 835-854,
726 2002.

Bauer, J. E., Cai, W.-J., Raymond, P. A., Bianchi, T. S., Hopkinson, C. S., and Regnier, P. A. G.: The changing carbon cycle of the coastal ocean, Nature, 504(7478), 61–70, 2013.

Beckler, J., Nuzzio, D., and Taillefert, M. : Development of single-step liquid chromatography methods with ultraviolet detection for the measurement of inorganic anions in marine waters, Limnol. Oceanogr. Meth., 12: 563–576, 2014.

Beckler, J. S., Kiriazis, N., Rabouille, C., Stewart, F. J., and Taillefert, M. : Importance of microbial iron reduction in deep sediments of river-dominated continental-margins, Mar. Chem., 178: 22–34, 2016.

Ben-Yaakov, S.: pH buffering of pore water of recent anoxic marine sediments, Limnol. Oceanogr., 18(1): 86–94, 1973.

Berelson, W.M. et al. : Biogenic matter diagenesis on the sea floor: A comparison between two continental margin transects, J. Mar. Res., 54: 731-762, 1996.

Berner, R. A. : Sedimentary pyrite formation, Am. J. Sci., 268, 1–23, 1970.

Berner, R. A. : Early Diagenesis: A Theoretical Approach, Princeton University Press, 1980.

Berner, R. A.: Burial of organic carbon and pyrite sulfur in the modern ocean; its geochemical and environmental significance, Am. J. Sci., 282, 451–473, 1982.

Bianchi, S. T. and Allison, M. A. : Large-river delta-front estuaries as natural ‘‘recorders’’ of global environmental change, Proc. Natl. Acad. Sci. U.S.A., 106, 8085–8092, 2009.

727 Bonin, P., Tamburini, C. and Michotey, V. : Determination of the bacterial processes which are
728 sources of nitrous oxide production in marine samples, Wat. Res. 36, 722–732, 2002.

Borowski, W. S., Pau, C. K., and Ussler, W. : Marine pore-water sulfate profiles indicate in situ methane flux from underlying gas hydrate, Geol., 24(7), 655–658, 1996.

729 Boudreau, B. P. and Jorgensen, B. B. : The Benthic Boundary Layer Transport Proceses
730 and Biogeochemistry, Oxford University Press, 198 Madison Avenue, New York, 2001.

Brenner, H., Braeckman, U., Le Guitton, M., and Meysman, F. J. R. : The impact of sedimentary alkalinity release on the water column CO_2 system in the North Sea, Biogeosci., 13, 841–863, 2016.

Bristow, G. and Taillefert, M. : VOLTINT: A Matlab $^{(R)}$-based program for semi-automated processing of geochemical data acquired by voltammetry, Comp. Geosci., 29, 153–162, 2008.

Broecker, W. S. and Peng, T.-H. : Gas exchange rates between air and sea, Tellus, 26, 21–35, 1974.

Buchholtz-Ten Brink, M. R., Gust, G., and Chavis, D. : Calibration and performance of a stirred benthic chamber. Deep-Sea Res., 36, 1083-1101, 1989.

Buffle, J. : Complexation reactions in aqueous systems: An Analytical Approach. Wiley and Sons, 1988.

Bura-Nakic, E., Viollier, E., Jezequel, D., Thiam, A., and Ciglenecki, I. : Reduced sulfur and iron species in anoxic water column of meromictic crater Lake Pavin (Massif Central, France), Chem. Geol., 266,311–317, 2009.

Burdige, D.J., Zimmerman, R.C.: Impact of sea grass density on carbonate dissolution in Bahamian sediments, Limnol. Oceanogr., 47, 1751-1763, 2002.

Burdige, D. : Burial of terrestrial organic matter in marine sediments: A re-assessment, Glob. Biogeochem. Cycles, 19, GB4011, doi:10.1029/2004/GB002368, 2005.

Burdige, D. : Estuarine and Coastal Sediments - Coupled Biogeochemical Cycling, Treat. Estuar. Coast. Sci., 5, 279–316, 2011.

Burdige, D. J. and Komada, T. : Anaerobic oxidation of methane and the stoichiometry of remineralization processes in continental margin sediments, Limnol. Oceanogr., 56(5), 1781–1796, 2011.

Cai, W.-J. : Estuarine and Coastal Ocean Carbon Paradox: CO_2 Sinks or Sites of Terrestrial Carbon Incineration?, Ann. Rev. Mar. Sci., 3(1), 123–145, 2011.

Cai, W.-J. and Reimers, C. E. : The development of pH and pCO_2 microelectrodes for studying the carbonate chemistry of pore waters near the sediment-water interface, Limnol. Oceanogr., 38,1762–1773, 1993.

Canfield, D. E., Jørgensen, B. B., Fossing, H., Glud, R., Gundersen, J., Ramsing, N. B., Thamdrup, B., Hansen, J. W., Nielsen, L. P., and Hall, P.O.J. : Pathways of organic carbon oxidation in three continental margin sediments, Mar. Geol., 113, 27–40, 1993a.

Canfield, D. E., Thamdrup, B., and Hansen, J. W. : The anaerobic degradation of organic matter in Danish coastal sediments: iron reduction, manganese reduction, and sulfate reduction, Geochim. Cosmochim. Acta, 57(16), 3867–3883, 1993b.

Carman, R. and Rahm, L. : Early diagenesis and chemical characteristics of interstitial water and sediments in the deep deposition bottoms of the Baltic proper. J. Sci. Res., 37, 25–47, 1997.

Cathalot, C., Rabouille, C., Pastor, L., Deflandre, B., Viollier, E., Buscail, R., Grémare, A., Treignier, C., and Pruski, A. : Temporal variability of carbon recycling in coastal sediments influenced by rivers: assessing the impact of flood inputs in the Rhône River prodelta, Biogeosci., 7,1187–1205, 2010.

Cathalot, C., Rabouille, C., Tisnérat-Laborde, N., Toussaint, F., Kerhervé, P., Buscail, R., Loftis, K., Sun, M.-Y., Tronczynski, J., Azoury, S., Lansard, B., Treignier, C., Pastor, L., and Tesi, T. : The fate of river organic carbon in coastal areas: A study in the Rhône River delta using multiple isotopic ($\delta^{13}C$, $\Delta^{14}C$) and organic tracers, Geochim. Cosmichim. Acta, 118,33–55, 2013.

Charmasson, S., Radakovitch, O., Arnaud, M., Bouisset, P., and Pruchon, A.-S. : Long-core profiles of ^{137}Cs, ^{134}Cs, ^{60}Co and ^{210}Pb in sediment near the Rhône River (Northwestern Mediterranean Sea), Estuaries, 21(3),367–378, 1998.

Chen, C.-T. A. and Borges, A. V. : Reconciling opposing views on carbon cycling in the coastal ocean: Continental shelves as sinks and near-shore ecosystems as sources of atmospheric CO_2, Deep-Sea. Res. II., 8, 578–590, 2009.

Clayton, T. D. and Byrne, R. H.: Spectrophotometric seawater pH measurements: total hydrogen ion concentration scale calibration of m-cresol purple and at-sea results, Deep-Sea. Res. I., 40(10), 2115–2129, 1993.

Cossarini, G., Lazzari, P., and Solidoro, C.: Spatiotemporal variability of alkalinity in the Mediterranean Sea, Biogeosci., 12, 1647–1658, 2015.

Cyronak, T., Santos, I.R., McMahon, A., Eyre, B.D.: Carbon cycling hysteresis in permeable carbonate sands over a diel cycle: Implications for ocean acidification, Limnol. Oceanogr., 58, 131-143, 2013.

Davison, W., Buffle, J., and DeVitre, R.: Voltammetric characterization of a dissolved iron sulphide species by laboratory and field studies, Anal. Chim. Acta, 377,193–203, 1998.

Dickson, A. G.: An exact definition of total alkalinity and a procedure for the estimation of alkalinity and total inorganic carbon from titration data, Deep-Sea. Res. A, 28 (6), 609–623, 1981.

Dickson, A.G., Sabine, C.L., Christian, J.R., : Guide to best practices for ocean CO_2 measurements. In: Dickson, A.G., Sabine, C.L., Christian, J.R. (Eds.), PICES Special Publication. 3. pp. 191, 2007.

Dumoulin, J.-P., Pozzato, L., Rassmann, J., Toussaint, F., Fontugne, M., Tisnérat-Laborde, N., Beck, L., Caffy, I., Delqué-Kolic, E., Moreau, C. and Rabouille, C. : Isotopic signature ($\delta^{13}C$, $\Delta^{14}C$) of DIC in sediment porewaters: an example from the Rhone River Delta, Radiocarbon 60, 1465-1481, 2018.

Estournel, C., Kondrachoff, V., Marsaleix, P., and Vehil, R. : The Plume of the Rhone: numerical simulation and remote sensing, Cont. Shelf. Res., 17(8), 899–924, 1997.

Ferron, S., Alonso-Perez, F., Ortega, T. and Forja, J.M. : Benthic respiration on the northeastern shelf of the Gulf of Cádiz, Mar. Ecol. Prog. Ser., 392, 69-80, 2009.

Friedl, G., Dinkel, C., and Wehrli, B. : Benthic fluxes of nutrients in the northwestern Black Sea, Mar. Chem., 62,77–88, 1998.

Gaillard, J.-F., Pauwels, H., and Michard, G. : Chemical diagenesis in coastal marine sediments, Oceanol. Acta, 12(3),173–187, 1989.

Got, H. and Aloisi, J. C. : The Holocene sedimentation on the Gulf of Lions margin: a quantitative approach, Cont. Shelf. Res., 10(9-11),841–855, 1990.

Grasshof, K., Ehrhardt, M. and Kremling, K,: Methods of Seawater Analysis, second revised and extended edition, Verlag Chemie GmbH, 420 pp, 1983.

Hammond, D.E., Fuller, C., Harmon, D., Hartman, B., Korosec, M., Miller, L.G., Real, R., Warren, S., Berelson, W. and Hager, S.W.: Benthic fluxes in San Francisco Bay, Hydrobiol., 129, 69-90, 1985.

Hammond, D.E., Giordani, P., Berelson, W.M. and Poletti, R.: Diagenesis of carbon and nutrients and benthic exchange in sediments of the Northern Adriatic Sea, Mar. Chem., 66, 53-79, 1999.

Hartnett, H. E., Keil, R. G., Hedges, J. I., and Devol, A. : Influence of oxygen exposure time on organic carbon preservation in continental margin sediments, Nature, 391,572–575, 1998.

Hedges, J. I. and Keil, R. G. : Sedimentary organic matter preservation: an assessment and speculative synthesis, Mar. Chem., 49,81–115, 1995.

Henneke, E., Luther, G., and Delange, G. : Determination of inorganic Sulfur Speciation with Polarographic Techniques - some preliminary Results for Recent Hypersaline Anoxic Sediments, Mar. Geol., 100,115–123, 1991.

Hu, X. and Cai, W.-J. : An assessment of ocean margin anaerobic processes on oceanic alkalinity budget, Glob. Biogeochem. Cycl., 25, 1–11, 2011a.

Hu, X. and Cai, W.-J. : The impact of denitrification on the atmospheric CO2 uptake potential of seawater, Mar. Chem., 127, 192-198, 2011b.

Hu, X. and Cai, W.J. : Estuarine acidification and minimum buffer zone—A conceptual study. Geophys. Res. Lett., 40, 5176–5181, 2013.

Jahnke, R. A. and Christiansen, M. B. : A free-vehicle benthic chamber instrument for sea floor studies, Deep-Sea. Res., 36(4), 625–637, 1989.

Jahnke, R. A. : A Global synthesis. In: Carbon and Nutrient Fluxes in Continental Margins, pages 597-615. K.-K. Liu, L. Atkinson, R. Quinones, L. Talaue-McManus (eds), Berlin, 2010.

Jiang, C. Z., Tosca, N. J. : Fe(II)-carbonate precipitation kinetics and the chemistry of anoxic ferruginous seawater, Earth Planet. Sci. Let. 506, 231–242, 2019.

Jones, M., Fennessey, C., DiChristina, T., and Taillefert, M. : Shewanella oneidensis MR-1 mutants selected for their inability to produce soluble organic-Fe(III) complexes are unable to respire Fe(III) as anaerobic electron acceptor, Envir. Microb., 12, 938–950, 2010.

Jørgensen, B. B. and Kasten, S. : Sulfur cycling and methane oxidation. In Marine Geochemistry. pp 271-310. Schulz H.D. et al. (eds), Springer Verlag, 2006.

Jourabchi, P., Van Cappellen, P., and Regnier, P. : Quantitative interpretation of pH distributions in aquatic sediments: A reaction-transport modeling approach, Amer. J. Sci., 305(9), 919–956, 2005.

Komada, T., Burdige, D. J., Li, H.-L., Magen, C., Chanton, J. P., and Cada, A. K. : Organic matter cycling across the sulfate-methane transition zone of the Santa Barbara Basin, California Borderland, Geochim. Cosmochim. Acta, 176, 259–278, 2016.

Krumins, V., Gehlen, M., Arndt, S., Van Cappellen, P., and Regnier, P. : Dissolved inorganic carbon and alkalinity fluxes from coastal marine sediments, model estimates for different shelf environments and sensitivity to global change, Biogeosci., 10(1), 371–398, 2013.

Lansard, B., Rabouille, C., Denis, L., and Grenz, C. : In situ oxygen uptake rates by coastal sediments under the influence of the Rhône River (NW Mediterranean Sea), Cont. Shelf. Res., 28(12), 1501–1510, 2008.

Lansard, B., Rabouille, C., Denis, L., and Grenz, C. : Benthic remineralization at the land–ocean interface: A case study of the Rhône River (NW Mediterranean Sea), Estuar. Coast. Shelf Sci., 81(4), 544–554, 2009.

Lehrter, J., Beddick, D., Devereux, R., Yates, D., and Murrel, M. : Sediment-water fluxes of dissolved inorganic carbon, O_2, nutrients, and N_2 from the hypoxic region of the Louisiana continental shelf, Biogeochem., 109 (1-3), 233–252, 2012.

Li, Y.-H. and Gregory, S. : Diffusion of ions in sea water and in deep-sea sediments, Geochim. Cosmochim. Acta, 38, 703–714, 1974.

Luecker, T.J., Dickson, A.G. and Keeling, C.D.: Ocean pCO2 calculated from dissolved inorganic carbon, alkalinity, and equations for K1 and K2: validation based on laboratory measurements of CO2 in gas and seawater at equilibrium, Mar. Chem., 70, 105-119, 2000.

Lukawska-Matuszewska, K.:Contribution of non-carbonate inorganic and organic alkalinity to total measured alkalinity in pore waters in marine sediments (Gulf of Gdansk, S-E Baltic Sea), Mar. Chem., 186, 211-220, http://dx.doi.org/10.1016/j.marchem.2016.10.002, 2016.

Łukawska-Matuszewska, K. and Graca, B.: Pore water alkalinity below the permanent halocline in the Gdańsk Deep (Baltic Sea) - Concentration variability and benthic fluxes, Mar. Chem., 204, 49-61, 2018.

Luther, G. W. and Ferdelman, T. : Voltametric Characterization of Iron (II) Sulfide Complexes in Laboratory Solutions and in Marine Waters and Porewaters, Environ. Sci. Technol., 27, 1154–1163, 1993.

Luther, G. W., Glazer, B., Ma, S., Trouwborst, R., Moore, T., Metzger, E., Kraiya, C., Waite, T., Druschel, G., Sundby, B., Taillefert, M., Nuzzio, D., Shank, T., Lewis, B., and Brendel, P. : Use of voltammetric solid-state (micro)electrodes for studying biogeochemical processes: Laboratory measurements to real time measurements with an in situ electrochemical analyzer(ISEA), Mar. Chem., 108,221–235, 2008.

Maillet, G.M. Vella, C., Berné, S., Friend, P. L., Amos, C. L., Fleury, T. J. and Normand, A. : Morphological changes and sedimentary processes induced by the December 2003 flood event at the present mouth of the Grand Rhône River (southern France), Mar. Geol., 234(1), 159-177, 2006.

McKee, B. A., Aller, R. C., Allison, M. A., Bianchi, T. S., and Kineke, G. C. : Transport and transformation of dissolved and particulate materials on continental margins influenced by major rivers: benthic boundary layer and seabed processes. Cont. Shelf. Res., 24, 899–926, 2004.

Millero, F.J.: The estimation of the pK^*_{HA} of acids in seawater using the Pitzer equations, Geochim. Cosmochim. Acta, 47, 2121-2129, 1983.

Millero, F. J : Thermodynamics of the carbon dioxide system in the oceans, Geochim. Cosmochim. Acta, 59, 661–677, 1995.

Miralles, J., Radakovitch, O., and Aloisi, J.-C. : ^{210}Pb sedimentation rates from the Nothwestern Mediterranean margin, Mar. Geol., 216,155–167, 2005.

Mucci, A : The solubility of calcite and aragonite in seawater at various salinities, temperatures and one atmosphere total pressure, Am. J. Sci., 283, 780–799, 1983.

Mucci, A., Sundby, B., Gehlen, M., Arakaki, T., Zhong, S., and Silverberg, N. : The fate of carbon in continental shelf sediments of eastern Canada: a case study, Deep-Sea Res. Part II: Topical Studies in Oceanography, 47,733–760, 2000.

Muller-Karger, F.E. et al.: The importance of continental margins in the global carbon cycle, Geophys. Res. Lett., 32, L01602, doi:10.1029/2004GL021346, 2005.

Murphy, J. and Riley, J. P. : A modified single solution method for determination of phosphate in natural waters, Anal. Chim. Acta, 27,31–36, 1962.

Nakayama, N., Tokieda, T., Suzuki, A., Kim, T., Gamo, T., and Obata, H. : Size fractionation of nanoparticulate metal sulfides in oxic water of Lake Teganuma, Japan, Geochem. J., 50,281–286, 2016.

Orr, J. C., Epitalon, J.-M., Dickson, A. G., and Gattuso, J.-P. : Routine uncertainty propagation for the marine carbon dioxide system, Mar. Chem., 207, 84-107, 2018

Ortega, T., Ponce, R., Forja, J. and Gomez-Parra, A. : Benthic fluxes of dissolved inorganic carbon in the Tinto-Odiel system (SW of Spain), Cont. Shelf. Res., 28, 458-469, 2008.

Pain, A.J., Martin, J.B. and Young, C.R. : Sources and sinks of CO2 and CH4 in siliciclastic subterranean estuaries, Limnol. Oceanogr. 64, 1500-1514, 2019.

Pastor, L., Cathalot, C., Deflandre, B., Viollier, E., Soetaert, E., Meysmann, K., Ulses, F. J. R., Metzger, C., and Rabouille, C. : Modeling biogeochemical processes in sediments from the Rhône River prodelta area (NW Mediterranean Sea), Biogeosci., 8,1351–1366, 2011.

Pastor, L., Rabouille, C., Metzger, E., Thibault de Chanvalon, A., Viollier, E. and Deflandre, B. : Transient early diagenetic processes in Rhône prodelta sediments revealed in contrasting flood events, Contin. Shelf Res. 166, 65-76, https://doi.org/10.1016/j.csr.2018.07.005, 2018.

Pierrot, D., Lewis, E. and Wallace, D.W.R.: MS Excel program developed for CO_2 system calculations. ORNL/CDIAC-105a. Carbon Dioxide Information Analysis Center, Oak Ridge National Laboratory, U.S. Department of Energy, Oak Ridge, Tennessee, 2006.

Pyzik, A. and Sommer, S. : Sedimentary Iron Monosulfides - Kinetics and Mechanism of Formation, Geochim. Cosmochim. Acta, 45,687–698, 1981.

Rabouille, C., Mackenzie, F. T. and Ver, L. M. : Influence of the human perturbation on carbon, nitrogen, and oxygen biogeochemical cycles in the global coastal ocean, Geochim. Cosmochim. Acta 65, 3615-3641, 2001.

Rabouille, C., Denis, L., Dedieu, K., Stora, G., Lansard, B., and Grenz, C. : Oxygen demand in coastal marine sediments: comparing in situ microelectrodes and laboratory core incubations, J. Exp. Mar. Biol. Ecol., 285,49–69, 2003.

Radakovitch, O., Cherry, R., and Heussner, S. : ^{210}Pb and ^{210}Po: tracers of particle transfer on the Rhône continental margin (NW Mediterranean), Deep S. Res. Part I: Oceanogr. Res. Pap., 46(9),1539–1563, 1999.

Rao, A.M.F., Malkin, S.Y., Montserrat, F. and Meysman, F.J.R. : Alkalinity production in intertidal sands intensified by lugworm bioirrigation, Estuar. Coast. shelf Sci., 148, 36-47, 2014.

Rassmann, J., Lansard, B., Pozzato, L., and Rabouille, C. : Carbonate chemistry in sediment pore waters of the Rhône River delta driven by early diagenesis (NW Mediterranean), Biogeosci., 13(18), 5379–5394, 2016.

Rickard, D. : Kinetics of FeS precipitation: Part 1. Competing reaction mechanisms, Geochim. Cosmochim. Acta., 59, 4367-4379, 1995.

Rickard, D. and Luther, G. W. : Kinetics of pyrite formation by the H_2S oxidation of iron(II) monosulfide in aqueous solutions between 25 and 125 °C: the mechanism, Geochim. Cosmochim. Acta, 61, 135–147, 1997.

Roussiez, V., Aloisi, J.-C., Monaco, A., and Ludwig, W. : 2005 Early muddy deposits along the Gulf of Lions shoreline: A key for a better understanding of land-to-sea transfer of sediments and associated pollutant fluxes, Mar. Geol., 222-223,345–358.

Rowe, G., Kaegi, M., Morse, J., Boland, G., and Briones, E. : Sediment community metabolism associated with continental shelf hypoxia, Northern Gulf of Mexico, Estuaries, 25, 1097–1106, 2002.

Rozan, T., Taillefert, M., Trouwborst, R., Glazer, B., Ma, S., Herszage, J., Valdes, L., Price, K., and Luther, G. : Iron-sulfur-phosphorus cycling in the sediments of a shallow coastal bay: Implications for sediment nutrient release and benthic macroalgal blooms, Limnol. Oceanogr., 47, 1346–1354, 2002.

Sarradin, P.-M. and Caprais, J.-C. : Analysis of dissolved gases by headspace sampling gas chromatography with column and detector switching: Preliminary results, Anal. Comm., 33,371–373, 1996.

Seeberg-Elverfeldt, J., Schlüter, M., Feseker, T., and Kölling, M. : Rhizon sampling of pore waters near the sediment/water interface of aquatic systems, Limnol. Oceanogr. Meth., 3,361–371, 2005.

Sempéré, R., Charrière, B., Wambeke, F. V., and Cauwet, G. : Carbon inputs of the Rhône River to the Mediterranean Sea: Biogeochemical implications, Glob. Biogeochem. Cycles, 14(2), 669–681, 2000.

Soetaert, K., Hofmann, A. F., Middelburg, J. J., Meysman, F. J. R., and Greenwood, J. : The effect of biogeochemical processes on pH, Mar. Chem., 105, 30–51, 2007.

Stookey, L. : Ferrozine - a new spectrophotometric reagent for iron, Anal. Chem., 42(7), 779–781, 1970.

Taillefert, M., Beckler, J., Carey, E., Burns, J., Fennessey, C., and DiChristina, T. : Shewanella putrefaciens produces an Fe(III)-solubilizing organic ligand during anaerobic respiration on insoluble Fe(III) oxides, J. Inorg. Biochem., 101, 1760–1767, 2007.

Taillefert, M., Bono, A. B., and Luther, G. W. : Reactivity of freshly formed Fe(III) in synthetic solutions and (pore)waters: Voltammetric evidence of an aging process, Environ. Sci. Technol., 34(11), 2169–2177, 2000.

Tercier-Waeber, M. and Taillefert, M. : Remote in situ voltammetric techniques to characterize the biogeochemical cycling of trace metals in aquatic systems, J. Environ. Monitor., 10, 30–54, 2008.

Theberge, S.M. and Luther III, G.W., : Determination of the electrochemical properties of a soluble aqueous FeS species present in sulfidic solutions, Aquat. Geochem., 3, 191-211, 1997.

Thomas, H., Schiettecatte, L.-S., Suykens, K., Koné, Y. J. M., Shadwick, E. H., Prowe, A. E. F., Bozec, Y., de Baar, H. J., and Borges, A. V. : Enhanced ocean carbon storage from anaerobic alkalinity generation in coastal sediments, Biogeosci., 6(2), 267–274, 2009.

Wolf-Gladrow, D. A., Zeebe, R. E., Klaas, C., Körtzinger, A., and Dickson, A. G. : Total alkalinity: The explicit conservative expression and its application to biogeochemical processes, Mar. Chem., 106, 287–300, 2007.

Zebracki, M., Eyrolle-Boyer, F., Evrard, O., Claval, D., Mourier, B., Gairoard, S., Cagnat, X. and Antonelli, C. : Tracing the origin of suspended sediment in a large Mediterranean river by combining continuous river monitoring and measurement of artificial and natural radionuclides, Sci. Tot. Environ., 502, 122-132, 2015.

Table 1. Individual and consecutive microbial and abiotic reactions that affect the theoretical ΔTA/ΔDIC (r_{AD}), ΔDIC/Δsulfate (r_{DS}), and ΔTA/Δsulfate (r_{AS}) stoichiometric ratios. Note that Eq. 14 and 17 include oxidation of H_2 by sulfate reducing bacteria.

	Individual Reactions	r_{AD} **ΔTA/ΔDIC**	r_{DS} **ΔDIC/ΔSO4**	r_{AS} **ΔTA/ΔSO4**
(1)	$Ca^{2+} + HCO_3^- \rightarrow CaCO_3 + H^+$	$\frac{-2}{-1} = 2$	-	-
(2)	$NH_4^+ + 2O_2 \rightarrow NO_3^- + 2H^+ + H_2O$	$\frac{-2}{0}$	-	-
(3)	$Fe^{2+} + \frac{1}{4}O_2 + \frac{5}{2}H_2O \rightarrow Fe(OH)_3 + 2H^+$	$\frac{-2}{0}$	-	-
(4)	$H_2S + 2O_2 \rightarrow SO_4^{2-} + 2H^+$	$\frac{-2}{0}$	-	$\frac{-2}{+1} = -2$
(5)	$CH_2O + \frac{4}{5}NO_3^- - \frac{2}{5}H^+ \rightarrow HCO_3^- + \frac{2}{5}N_2 + \frac{2}{5}H_2O$	$\frac{+4/5}{+1} = 0.8$	-	-
(6)	$2CH_2O + SO_4^{2-} \rightarrow 2HCO_3^- + H_2S$	$\frac{+2}{+2} = 1$	$\frac{+2}{-1} = -2$	$\frac{+2}{-1} = -2$
(7)	$CH_2O + 4\,Fe(OH)_3 + 7H^+ \rightarrow HCO_3^- + 4\,Fe^{2+} + 10\,H_2O$	$\frac{+8}{+1} = 8$	-	-
(8)	$CH_4 + SO_4^{2-} + H^+ \rightarrow HCO_3^- + H_2S + H_2O$	$\frac{+2}{+1} = 2$	$\frac{+1}{-1} = -1$	$\frac{+2}{-1} = -2$
(9)	$Fe(OH)_{3(s)} + \frac{1}{2}H_2S + 2H^+ \rightarrow Fe^{2+} + \frac{1}{2}S(0) + 3H_2O$	$\frac{+2}{0}$	-	-
(10)	$Fe^{2+} + H_2S \rightarrow FeS_{(s)} + 2H^+$	$\frac{-2}{0}$	-	-
(11)	$FeS_{(s)} + H_2S \rightarrow FeS_{2(s)} + H_2$	$\frac{0}{0}$	-	-
	Consecutive Reactions	r_{AD} **ΔTA/ΔDIC**	r_{DS} **ΔDIC/ΔSO4**	r_{AS} **ΔTA/ΔSO4**
	Sulfate reduction, abiotic reduction of Fe(III) oxides, and precipitation of sulfide minerals			
(12)	$2CH_2O + SO_4^{2-} + \frac{2}{3}Fe(OH)_{3(s)} \rightarrow 2HCO_3^- + \frac{1}{3}S(0) + \frac{2}{3}FeS_{(s)} + 2H_2O$	$\frac{+2}{+2} = 1$	$\frac{+2}{-1} = -2$	$\frac{+2}{-1} = -2$
(13)	$2CH_2O + SO_4^{2-} + \frac{2}{5}Fe(OH)_{3(s)} \rightarrow 2HCO_3^- + \frac{1}{5}S(0) + \frac{2}{5}FeS_{2(s)} + \frac{6}{5}H_2O + \frac{2}{5}H_2$	$\frac{+2}{+2} = 1$	$\frac{+2}{-1} = -2$	$\frac{+2}{-1} = -2$
(14)	$\frac{20}{11}CH_2O + SO_4^{2-} + \frac{4}{11}Fe(OH)_{3(s)} + \frac{2}{11}H^+ \rightarrow \frac{20}{11}HCO_3^- + \frac{2}{11}S(0) + \frac{4}{11}FeS_{2(s)} + \frac{1}{11}H_2S + \frac{16}{11}H_2O$	$\frac{+2}{+20/11} = 1.1$	$\frac{+20/11}{-1} = -1.8$	$\frac{+2}{-1} = -2$
	Concomitant dissimilatory iron and sulfate reduction with precipitation of sulfide minerals			

(15)	$\frac{9}{4}CH_2O + SO_4^{2-} + Fe(OH)_{3(s)} \rightarrow \frac{9}{4}HCO_3^- + \frac{1}{4}H^+ + FeS_{(s)} + \frac{5}{2}H_2O$	$\frac{+2}{+9/4} = 0.89$	$\frac{+9/4}{-1} = -2.25$	$\frac{+2}{-1} = -2$
(16)	$\frac{17}{8}CH_2O + SO_4^{2-} + \frac{1}{2}Fe(OH)_{3(s)} \rightarrow \frac{17}{8}HCO_3^- + \frac{1}{8}H^+ + \frac{1}{2}FeS_{2(s)} + \frac{5}{4}H_2O + \frac{1}{2}H_2$	$\frac{+2}{+17/8} = 0.94$	$\frac{+17/8}{-1} = -2.13$	$\frac{+2}{-1} = -2$
(17)	$\frac{17}{9}CH_2O + SO_4^{2-} + \frac{4}{9}Fe(OH)_{3(s)} + \frac{1}{9}H^+ \rightarrow \frac{17}{9}HCO_3^- + \frac{4}{9}FeS_{2(s)} + \frac{1}{9}H_2S + \frac{14}{9}H_2O$	$\frac{+2}{+17/9} = 1.06$	$\frac{+17/9}{-1} = -1.89$	$\frac{+2}{-1} = -2$

Table 2. Sampling sites during the AMOR-B-Flux cruise in September 2015 and main characteristics of bottom waters; dist. = distance to the Rhône River mouth; ω = sedimentation rate; Station Z was sampled twice (Z on 09/08/15 and Z' on 09/14/15) to investigate spatial variability; n.d. = not determined.

Domain	**Proximal**			**Prodelta**			**Distal**
Stations	**A**	**Z**	**Z'**	**AK**	**B**	**K**	**E**
Long. ° E	4.85	4.868	4.868	4.853	4.833	4.858	4.684
Lat. °N	43.311	43.318	43.318	43.307	43.305	43.301	43.22
Dist. [km]	2.1	2.2	2.2	2.8	3	3.3	14.3
Depth [m]	20	20	20	42	50	58	72.5
Temp. [°C]	16.3	19.6	14.7	16.2	20.6	14.7	14.3
Salinity	37.5	37.6	37.7	37.7	38.0	37.7	37.8
O_2 [µM]	253.1 ± 0.3	249.5 ± 0.3	242.6 ± 0.2	250.2 ± 0.1	n.d.	241.8 ± 0.2	221.5 ± 0.3
DIC [mM]	2.29 ± 0.01	2.31 ± 0.01	n.d.	2.28 ± 0.01	2.27 ± 0.01	2.31 ± 0.01	2.33 ± 0.01
TA [mM]	2.61 ± 0.02	2.60 ± 0.01	n.d.	2.60 ± 0.02	2.60 ± 0.01	2.60 ± 0.02	2.61 ± 0.01
pH_T	8.08 ± 0.01	8.06 ± 0.01	8.09 ± 0.01	8.09 ± 0.01	8.07 ± 0.01	8.08 ± 0.01	8.05 ± 0.01
mean ϕ	0.69 ± 0.04	0.65 ± 0.04	0.65 ± 0.04	0.68 ± 0.02	0.66 ± 0.03	0.65 ± 0.05	0.64 ± 0.04
w [cm yr^{-1}]		30 - 40[a]			1 - 4[b]		0.1 - 1[c]
	Benthic fluxes (mmol m^{-2} d^{-1})						
TA flux	14.3 ± 1.6	73.9 ± 20.6	56.0 ± 17.8	n.d.	n.d.	n.d.	3.7 ± 0.9
DIC flux	17.8 ± 1.6	78.3 ± 10.9	37.2 ± 7.2	n.d.	n.d.	n.d.	9.9 ± 0.9
DOU	10.2 ± 1.3	10.4 ± 0.9	n.d.	n.d.	n.d.	5.9 ± 1.0	3.6 ± 0.6

a. Data from Charmasson et al., 1998
b. Data from Lansard et al., 2009
c. Data from Miralles et al., 2005

Table 3. Diffusion-corrected stoichiometric ratios r_{AD} , r_{DS}, and r_{AS} and their corresponding ratios corrected for carbonate precipitation (r_{ADc} , r_{DSc}, and r_{ASc}) along with their associated determination coefficients (r^2) from linear regression; n.d = not determined.

Stations	**A**	**Z**	**AK**	**B**	**K**	**E**
r_{AD}	0.99 ± 0.01	1.08 ± 0.02	1.02 ± 0.02	1.02 ± 0.01	0.98 ± 0.05	0.90 ± 0.04
r^2	0.998	0.997	0.998	0.999	0.986	0.984
r_{ADc}	1.10 ± 0.01	1.16 ± 0.03	1.07 ± 0.02	1.15 ± 0.02	1.06 ± 0.07	1.15 ± 0.11
r^2	0.999	0.997	0.996	0.998	0.974	0.885
r_{DS}	-1.67 ± 0.06	-1.87 ± 0.17	-1.85 ± 0.05	-1.18 ± 0.05	-1.72 ± 0.03	n.d.
r^2	0.990	0.969	0.995	0.988	0.997	n.d.
r_{DSc}	-1.88 ± 0.05	-2.05 ± 0.18	-1.95 ± 0.05	-1.37 ± 0.05	-1.86 ± 0.07	n.d.
r^2	0.994	0.972	0.996	0.990	0.994	n.d.
r_{AS}	-1.66 ± 0.07	-2.03 ± 0.17	-1.89 ± 0.06	-1.21 ± 0.04	-1.69 ± 0.07	n.d.
r^2	0.986	0.973	0.992	0.994	0.991	n.d.
r_{ASc}	-2.07 ± 0.05	-2.35 ± 0.14	-2.01 ± 0.06	-1.58 ± 0.05	-1.89 ± 0.14	n.d.
r^2	0.994	0.977	0.989	0.992	0.958	n.d.

Table 4. Calculated FeS burial fluxes and their TA-equivalent production at each station compared to measured TA benthic fluxes; n.d. = not determined.

Stations	**A and Z**	**AK**	**E**
ω [cm yr^{-1}]	30	3	0.1
ϕ	0.67	0.68	0.64
Mean [AVS] [µmol g^{-1}]	19.5 ± 4.9	45.0 ± 11.3	9.0 ± 2.3
sediment density [g cm^{-3}]	2.5	2.5	2.5
FeS burial flux [mmol S m^{-2} d^{-1}]	12.5 ± 3.8	4.9 ± 1.4	0.02 ± 0.01
TA-equivalent prod. (=2.0 FeS) [mmol TA m^{-2} d^{-1}]	25 ± 8	9.8 ± 2.8	0.04 ± 0.1
Measured TA flux at SWI [mmol TA m^{-2} d^{-1}]	14.3 - 73.9	n.d.	3.7 ± 0.9

740 **Figure Captions**

741 **Figure 1:** Map of the Rhône River prodelta with the stations investigated during the AMOR-B-Flux
742 cruise in September 2015.

743

744 **Figure 2:** Dissolved oxygen and pH microprofiles recorded *in situ* at the sediment-water interface
745 at stations A, Z, K, and E. Stations A and Z are located in the proximal zone, K in the prodelta, and
746 E in the distal zone (i.e. continental shelf).

747

748 **Figure 3:** DIC and TA fluxes measured with the benthic chamber and diffusive oxygen uptake
749 (DOU) rates calculated from *in situ* microelectrode depth profiles at stations A, Z (measured during
750 two deployments), and E. Error bars represent either uncertainties about the linear regression of the
751 benthic DIC and TA gradients taking into account individual error bars of each data point or error
752 propagation and standard deviations of multiple DOU measurements. Fluxes out of the sediment are
753 positive and fluxes into the sediment are negative.

754

755 **Figure 4:** Depth profiles of dissolved O_2, Mn^{2+}, Fe^{2+}, org-Fe(III), FeS_{aq}, and ΣH_2S concentrations
756 measured electrochemically in intact sediment cores at stations A, Z, AK, K, B, and E. Org-Fe(III)
757 and FeS_{aq} are reported in normalized current intensities (nA).

758

759 **Figure 5:** Depth profiles of pore water TA, DIC, SO_4^{2-}, NH_4^+, CH_4, Ca^{2+}, nanoparticulate FeS
760 (FeS_0), ΣPO_4^{3-}, and AVS concentrations along with the calcium carbonate (calcite) saturation state
761 of the pore waters (Ω_{Ca}) at stations A, Z, AK, K, B, and E. Alternating symbol shapes indicate data
762 collected from duplicate long and short sediment cores. The calcium carbonate (calcite) saturation
763 state (Ω_{Ca}) and pore water FeS_0 concentrations were calculated whereas AVS was determined from
764 solid phase extractions. The two horizontal lines identify the sulfate-methane transition zone

765 (SMTZ) found at stations A and Z. Error bars represent standard deviations of multiple
766 measurements for the concentrations and error propagation for Ω. Concentrations of CH_4 were not
767 measured at stations B, K, and E.
768
769 **Figure 6:** Average pore water saturation states with respect to calcite and aragonite in the first
770 centimetre of the sediment at stations: a- Proximal (St. A, Z), b- prodelta (St. K), and c- distal (St.
771 E) calculated using the DIC gradients at the SWI together with the average measured pH
772 microprofiles.
773
774 **Figure 7:** Current intensities of organic-Fe(III) complexes as a function of Fe^{2+} concentrations
775 measured at each depth at stations A, Z, AK, B, and K compared to the same data obtained from
776 iron-rich deep-sea sediments (Beckler et al., 2016).
777
778 **Figure 8:** Conceptual model to visualize the link between the burial of iron sulfide minerals and
779 benthic alkalinity fluxes in case of low sedimentation and OC flux (black) and high sedimentation
780 rates and OC flux (red). The total alkalinity (TA) produced under anaerobic conditions at depth
781 diffuses upwards towards the aerobic sediment layer where it is consumed during reoxidation of
782 Fe^{2+} and ΣH_2S by dissolved oxygen (black). If the precipitation of sulfide minerals is significant,
783 the reduced iron and sulfide metabolites produced during anaerobic respiration are not reoxidized
784 by dissolved oxygen, and the TA produced is able to reach the bottom waters (red). The intensity of
785 the alkalinity flux into the bottom waters is indicated by the thickness of the arrow at the SWI.
786
787 **Figure 9:** TA to DIC benthic flux ratios as a function of depth at stations A, Z, and E of the Rhône
788 River delta compared to different coastal regions of water depth < 100 m where this ratio was
789 quantified from *in situ* benthic flux measurements (modified from Hu and Cai, 2011b). Other
790 coastal regions include Cadiz Bay and the Guadalquivir continental shelf (Spain; Ferron et al.,

2009), the Rio Tinto estuary (Spain; Ortega et al., 2008), the Po river delta and nearby Adriatic shelf (Italy; Hammond et al. 1999), San Francisco Bay (USA; Hammond et al., 1985), and the California shelf (USA; Berelson et al., 1996). The global coastal average TA to DIC flux ratio predicted from Krumins et al., 2013 is also reported for reference. Note that this average is different from that reported by Hu and Cai (2011b) which was corrected in their later publication (Hu and Cai, 2013).

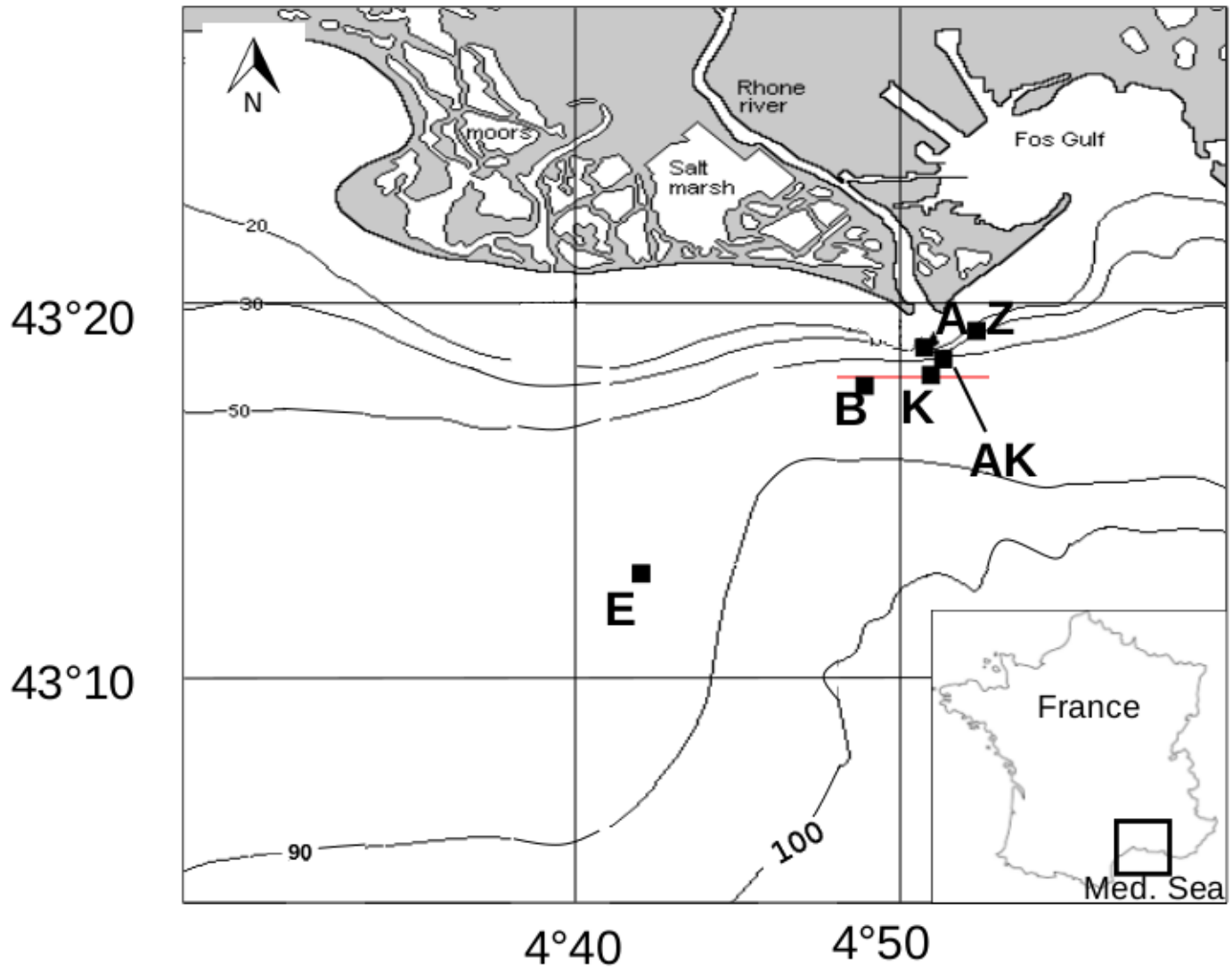
N
moors
Rhone river
Salt marsh
Fos Gulf
20
30
50
90
100
A
Z
B
K
AK
E
France
Med. Sea
43°20
43°10
4°40
4°50

Figure.1

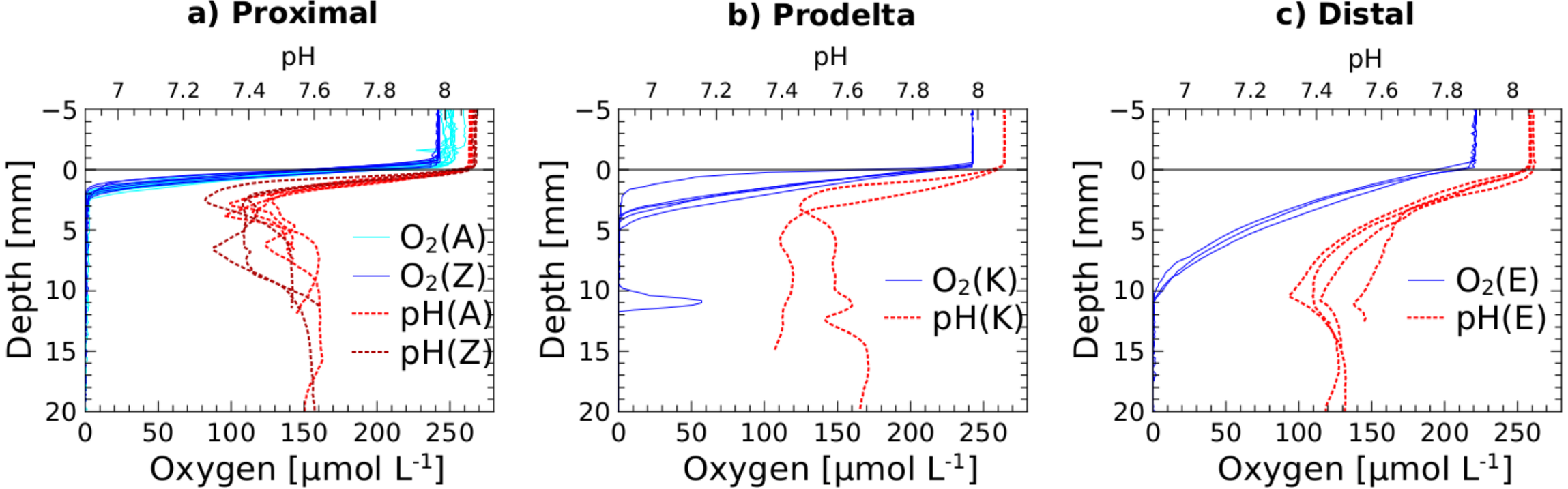
a) Proximal
b) Prodelta
c) Distal
pH
7
7.2
7.4
7.6
7.8
8
Depth [mm]
−5
0
5
10
15
20
O2(A)
O2(Z)
pH(A)
pH(Z)
O2(K)
pH(K)
O2(E)
pH(E)
0
50
100
150
200
250
Oxygen [µmol L-1]

Figure.2

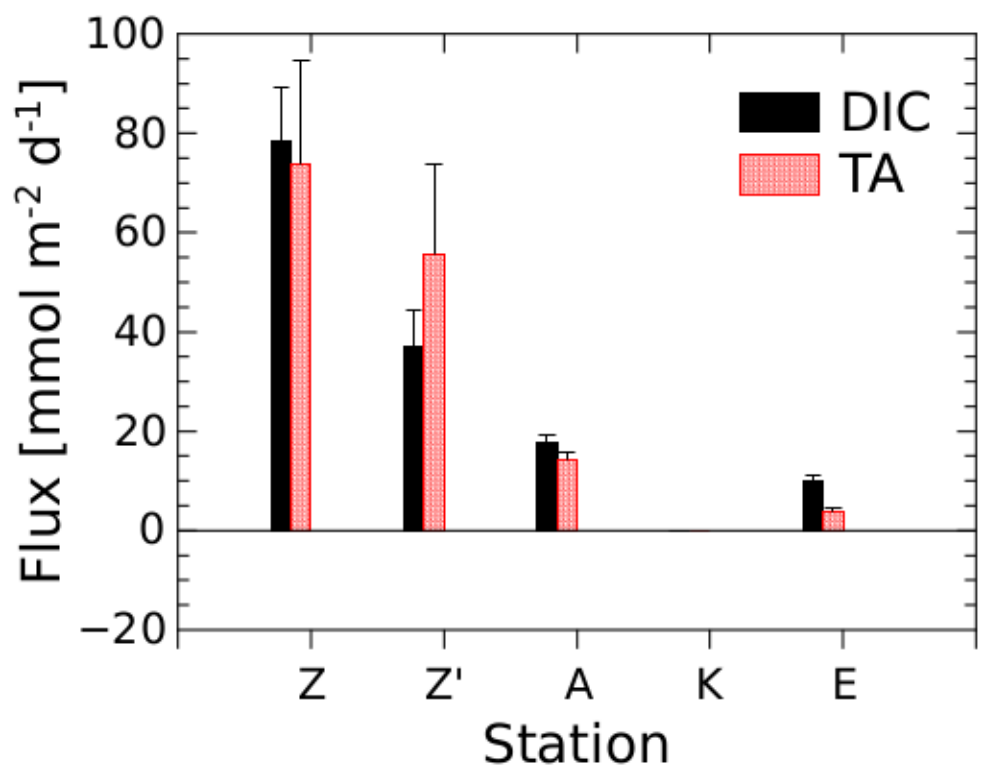
DIC
TA
Flux [mmol m-2 d-1]
100
80
60
40
20
0
−20
Z
Z'
A
K
E
Station

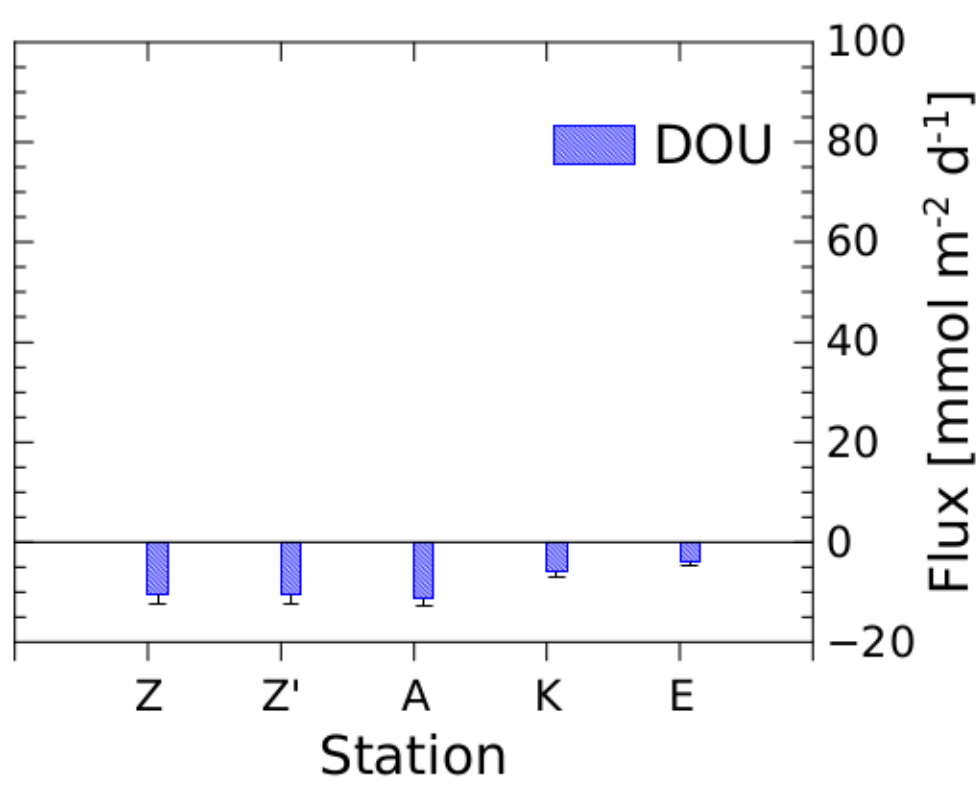
DOU
Flux [mmol m-2 d-1]
100
80
60
40
20
0
−20
Z
Z'
A
K
E
Station

Figure.3

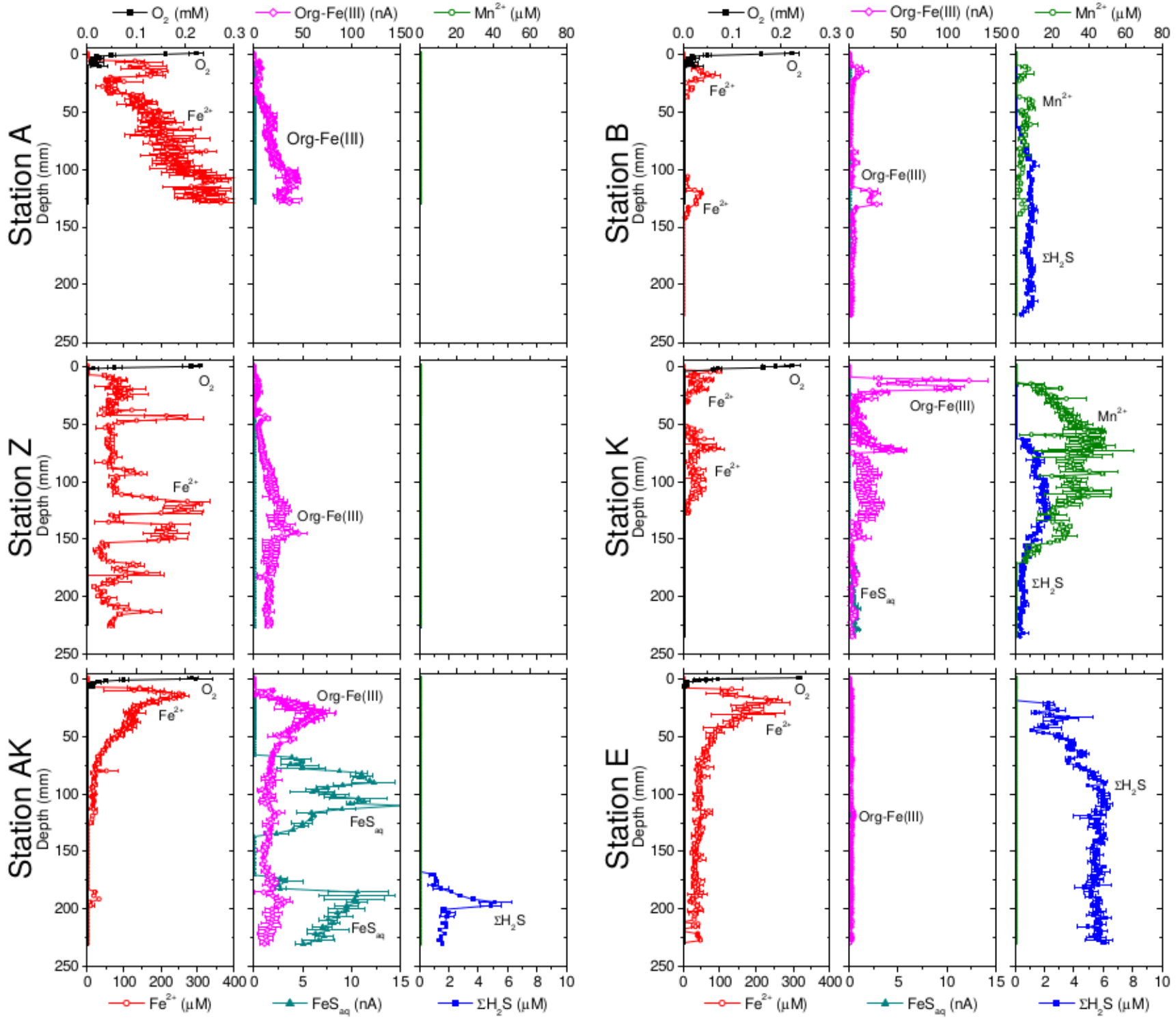
Station A
Station Z
Station AK
Station B
Station K
Station E
Depth (mm)
O2 (mM)
Org-Fe(III) (nA)
Mn2+ (μM)
Fe2+ (μM)
FeSaq (nA)
ΣH2S (μM)
O2
Fe2+
Org-Fe(III)
Mn2+
FeSaq
ΣH2S

Figure.4

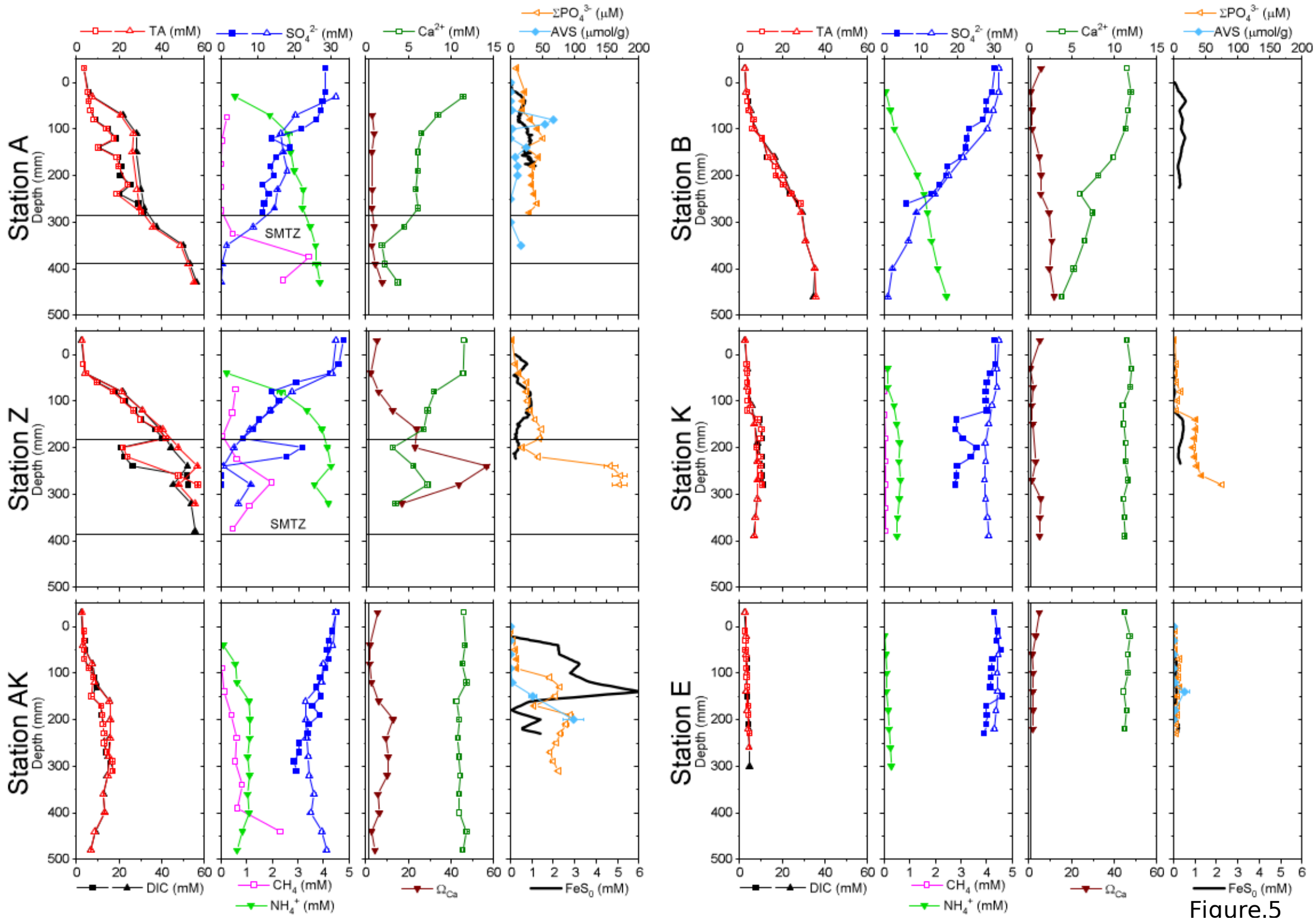
Station A
Station Z
Station AK
Station B
Station K
Station E
Depth (mm)
TA (mM)
SO4 2- (mM)
Ca2+ (mM)
ΣPO4 3- (μM)
AVS (μmol/g)
SMTZ
DIC (mM)
CH4 (mM)
NH4+ (mM)
ΩCa
FeS0 (mM)

Figure.5

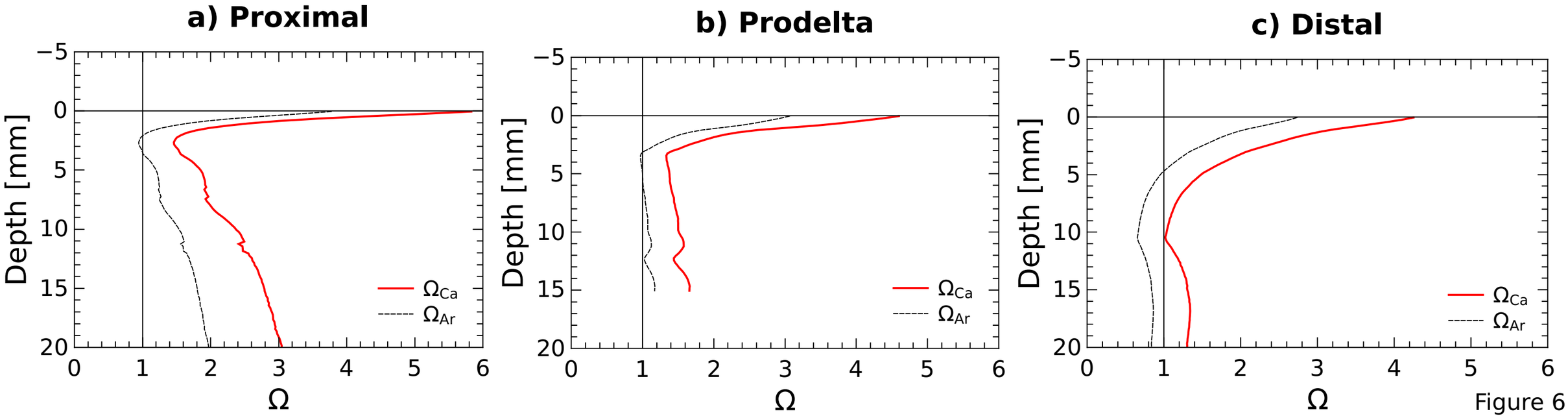
a) Proximal
b) Prodelta
c) Distal
Depth [mm]
Ω
Ω_{Ca}
Ω_{Ar}
−5
0
5
10
15
20
0
1
2
3
4
5
6

Figure 6

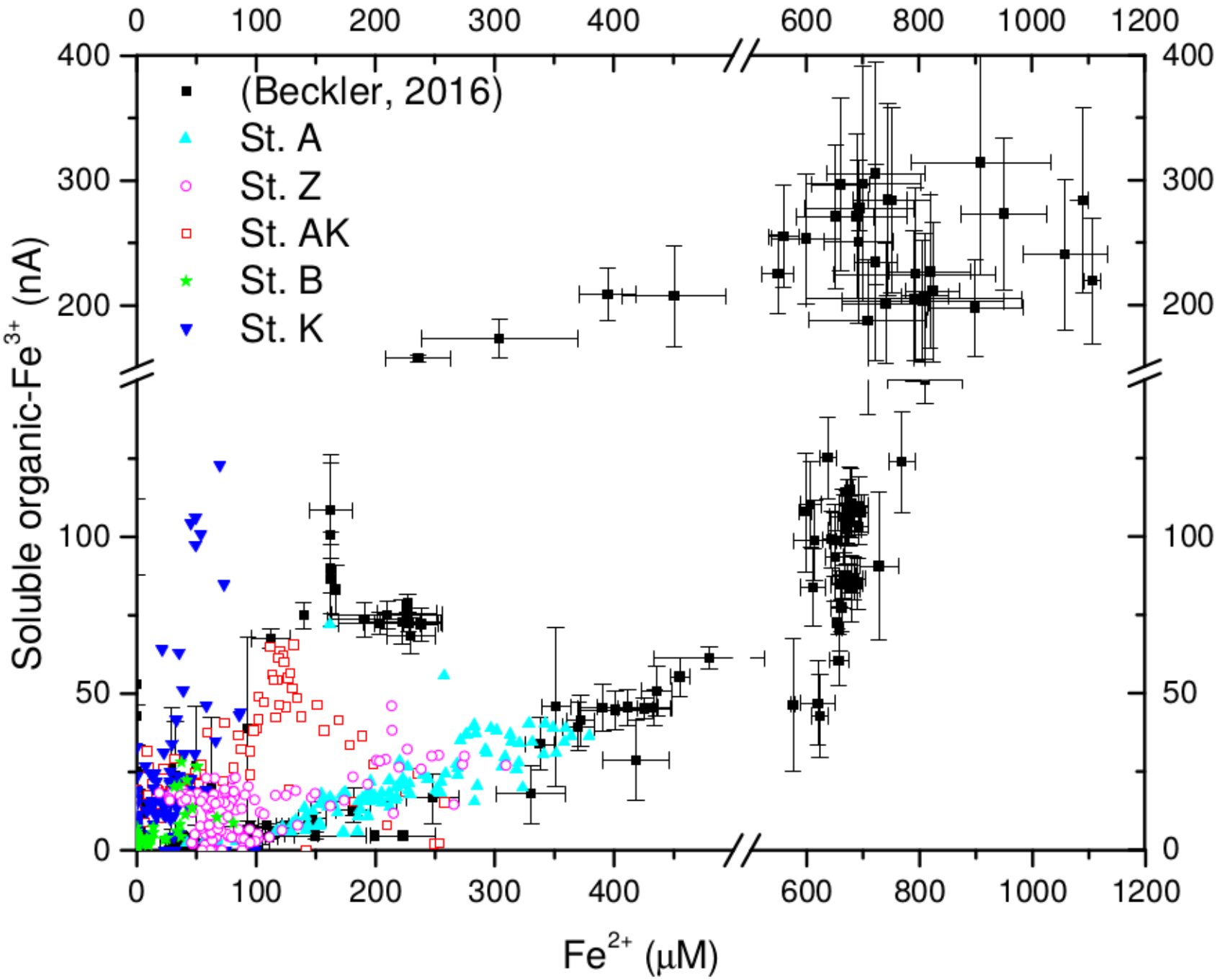
(Beckler, 2016)
St. A
St. Z
St. AK
St. B
St. K
Soluble organic-Fe3+ (nA)
Fe2+ (μM)
0
100
200
300
400
600
800
1000
1200
50

Figure.7

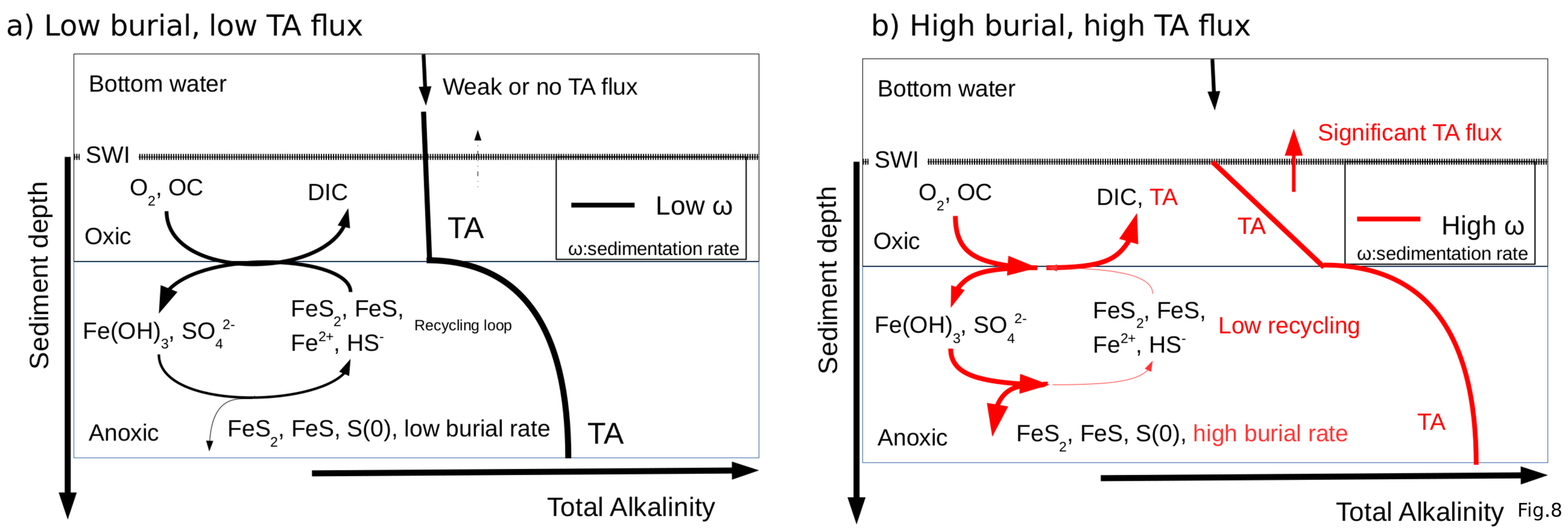
a) Low burial, low TA flux
Bottom water
Weak or no TA flux
SWI
O2, OC
DIC
Oxic
TA
Low ω
ω:sedimentation rate
Sediment depth
Fe(OH)3, SO4 2-
FeS2, FeS,
Fe2+, HS-
Recycling loop
Anoxic
FeS2, FeS, S(0), low burial rate
TA
Total Alkalinity
b) High burial, high TA flux
Bottom water
Significant TA flux
SWI
O2, OC
DIC, TA
TA
Oxic
High ω
ω:sedimentation rate
Sediment depth
Fe(OH)3, SO4 2-
FeS2, FeS,
Fe2+, HS-
Low recycling
Anoxic
FeS2, FeS, S(0), high burial rate
TA
Total Alkalinity

Fig.8

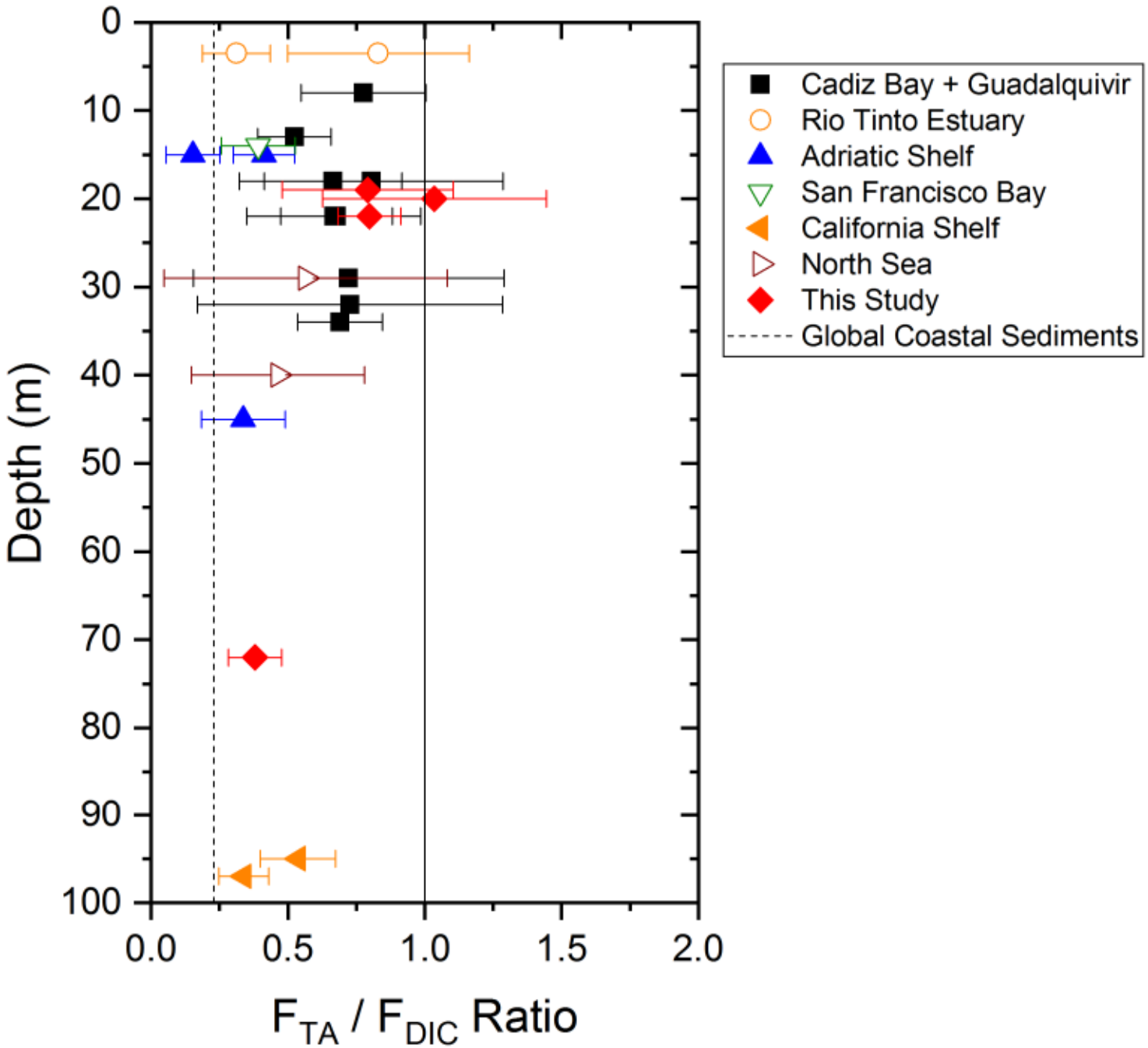
Depth (m)
0
10
20
30
40
50
60
70
80
90
100
0.0
0.5
1.0
1.5
2.0
F_{TA} / F_{DIC} Ratio
Cadiz Bay + Guadalquivir
Rio Tinto Estuary
Adriatic Shelf
San Francisco Bay
California Shelf
North Sea
This Study
Global Coastal Sediments

Figure.9

Supplementary Material:

Benthic alkalinity and DIC fluxes in the Rhône River prodelta generated by decoupled aerobic and anaerobic processes

Jens Rassmann[a,1], Eryn M. Eitel[b,1], Cécile Cathalot[c], Christophe Brandily[c], Bruno Lansard[a] , Martial Taillefert[b] , Christophe Rabouille[a, 2]

[a] *Laboratoire des Sciences du Climat et de l'Environnement, LSCE/IPSL,CEA-CNRS-UVSQ-Université Paris Saclay, 91198 Gif-sur-Yvette, France*
[b] *School of Earth and Atmospheric Sciences; Georgia Institute of Technology, GA 30332-0340 Atlanta, USA*
[c] *IFREMER, Laboratoire Environnement Profond, 29280 Plouzané, France*

[1] Jens Rassmann and Eryn M. Eitel contributed equally to this article
[2] Corresponding author
Email adress: rabouill@lsce.ipsl.fr (Christophe Rabouille)
ORCID: https://orcid.org/0000-0003-1211-717X

S1. Linear increase of TA and DIC concentrations with time in the benthic chamber

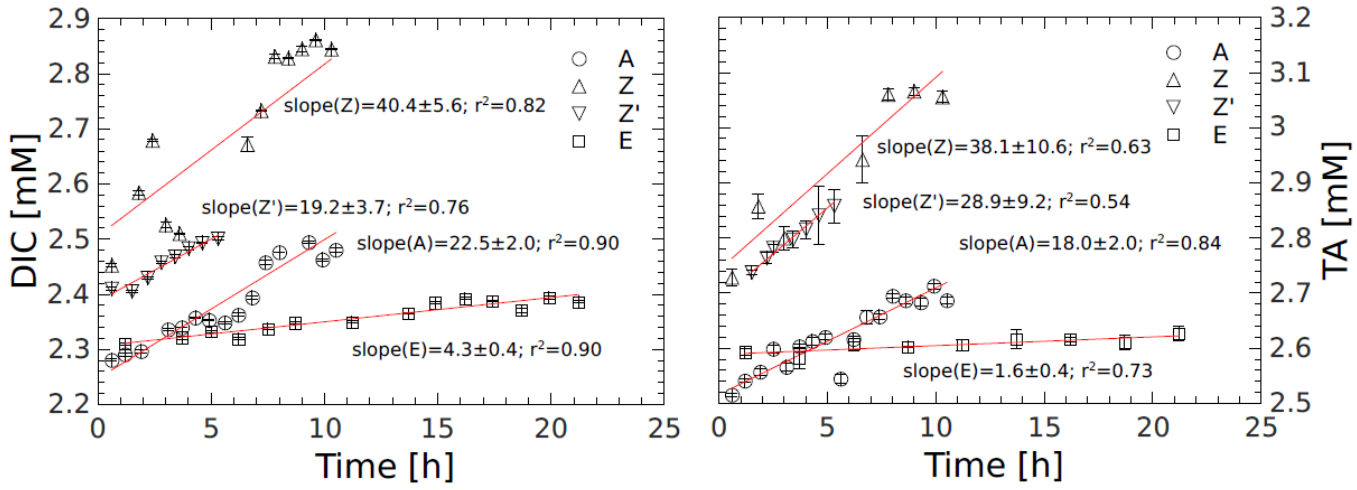

Figure S1: *Temporal evolution of DIC and total alkalinity concentrations in the benthic chamber at stations A, Z (measured during two deployments), and E. Error bars represent analytical uncertainties determined from triplicate measurements. The benthic fluxes and their standard deviations are provided in the text, in Figure 4 and in Table 2.*

S2. Ion activity product for FeS precipitation

The ionic activity product (IAP) for the precipitation of $FeS_{(s)}$ was calculated using following Beckler et al. (2016),

$$pIAP = \log\left(\frac{\gamma_{Fe(II)}[Fe^{2+}]\gamma_{\mathrm{HS}}\alpha_{\mathrm{HS}}\Sigma H_2S}{\{H^+\}}\right)$$

where $\gamma_{Fe(II)}$ and γ_{HS} represent the activity coefficients of Fe^{2+} and HS^-, $\alpha_{HS} = \frac{\{H^+\}K_{a1}}{\{H^+\}^2+\{H^+\}K_{a1}+K_{a1}K_{a2}}$ is calculated with the acid dissociation constant of H_2S ($K_{a1} = 10^{-6.88}$) and HS^- ($K_{a2} = 10^{-17}$) (Davison, 1991), and $\{H^+\}$ is the activity of the proton. Activity coefficients of Fe^{2+} (Millero and Schreiber, 1982) and HS^- (Millero, 1983) were calculated using Pitzer parameters. The measured Fe^{2+} concentrations were used as 'free' available Fe^{2+}, as Fe^{2+}

does not form strong complexes, and $\sum H_2S$ concentrations were used to calculate the speciation of sulfide species (assuming no elemental sulfur or polysulfide were present in the pore waters). The ion activity products (pIAPs) calculated at most stations indicate that pore waters were either undersaturated, as a result of the low concentrations (stations AK, B, and K) or complete absence (stations A and Z) of dissolved sulfides, or close to the solubility of amorphous FeS or mackinewite (Fig. S2). These findings are surprising given the presence of significant concentrations of nanoparticulate FeS (FeS_0) in the pore waters at each of these stations (Fig. 6). The large FeS_0 concentration in the pore waters suggests that iron sulfide particles were already aggregated at the time of sampling but not totally precipitated as $FeS_{(s)}$. These findings therefore indicate that these sediments were not at equilibrium and provide another piece of evidence for a highly dynamic system.

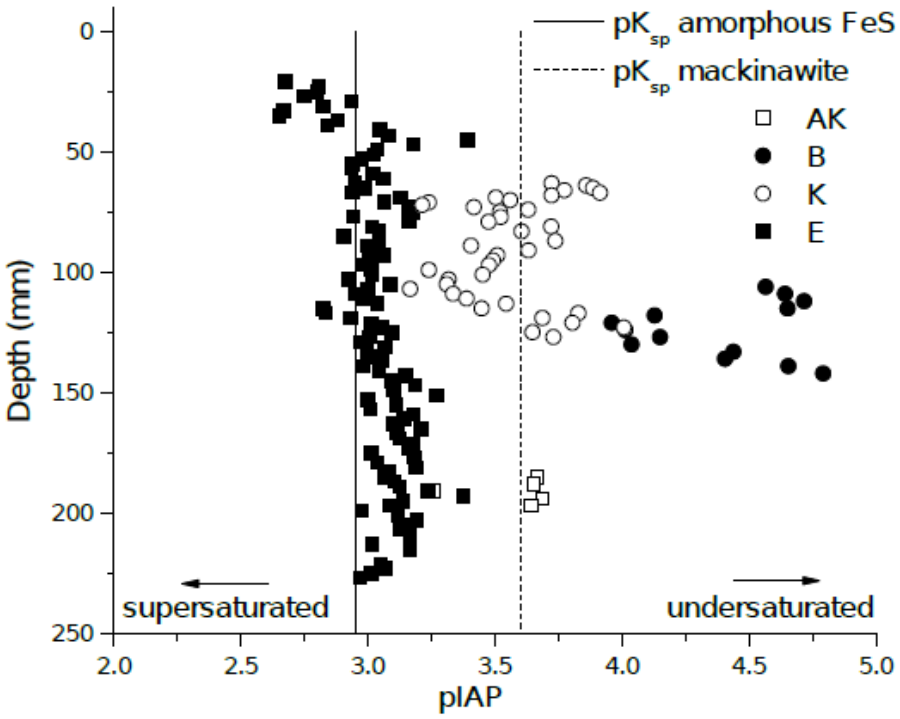

Figure S2: *Calculated pIAP values as a function of depth into the sediment compared to the* pK_{sp} *of amorphous FeS and mackinawite. Due to the lack of dissolved sulfide, the pIAP values in the pore waters of station A and Z could not be calculated.*

References

Beckler, J. S., Kiriazis, N., Rabouille, C., Stewart, F. J., and Taillefert, M. (2016). Importance of microbial iron reduction in deep sediments of river-dominated continental-margins. *Mar. Chem*., 178: 22–34.

Davison, W., 1991. The solubility of iron sulphides in synthetic and natural waters at ambient temperature. *Aquat. Sci.*, 53(4): 309-329.

Millero, F.J., 1983. The estimation of the pK^*_{HA} of acids in seawater using the Pitzer equations. *Geochim. Cosmochim. Acta*, 47: 2121-2129.

Millero, F.J. and Schreiber, D.R., 1982. Use of the ion pairing model to estimate activity coefficients of the ionic components of natural waters. *Am. J. Sci*., 282: 1508-1540.